

Influence of gas compression on flame acceleration in the early stage of burning in tubes

Damir Valiev^{a,b}, V'yacheslav Akkerman^a, Mikhail Kuznetsov^c,
Lars-Erik Eriksson^d, Chung K. Law^a, and Vitaly Bychkov^b

^a*Department of Mechanical and Aerospace Engineering,
Princeton University, Princeton, NJ 08544-5263, USA*

^b*Department of Physics, Umeå University, 90187 Umeå, Sweden*

^c*Institute for Nuclear and Energy Technologies,*

Karlsruhe Institute of Technology, Kaiserstrasse 12, 76131 Karlsruhe, Germany

^d*Department of Applied Mechanics, Chalmers University of Technology, 41296 Göteborg, Sweden*

Abstract

The mechanism of finger flame acceleration at the early stage of burning in tubes has been observed experimentally by Clanet and Searby [Combust. Flame 105: 225 (1996)] for slow propane-air flames, and elucidated analytically and computationally by Bychkov et al. [Combust. Flame 150: 263 (2007)] in the limit of an incompressible flow. We analytically, experimentally and computationally study herein the finger flame acceleration for fast burning flames, when the gas compressibility assumes an important role. Specifically, we have developed a theory through small Mach number expansion up to the first-order terms, demonstrating that gas compression reduces the acceleration rate and thereby moderates the finger flame acceleration noticeably. We have also conducted experiments for hydrogen-oxygen mixtures with considerable initial values of the Mach number, showing finger flame acceleration with the acceleration rate much smaller than those obtained previously for hydrocarbon flames. Furthermore, we have performed numerical simulations for a wide range of initial laminar flame velocities, with the results substantiating the experiments. It is shown that the theory is in good quantitative agreement with numerical simulations for small gas compression (small initial flame velocities). Similar to previous works, the numerical simulation shows that finger flame acceleration is followed by formation of the “tulip” flame, which indicates termination of the early acceleration process.

Nomenclature

c_S	sound speed
C_P	heat capacity at constant pressure
C_V	heat capacity at constant volume
E_a	activation energy
Le	Lewis number
L_f	flame thickness
L_w	flame length in a 2D configuration
Ma	initial flame propagation Mach number ($Ma = S_L/c_{S,0}$)
P	pressure
Pr	Prandtl number
q_i	energy diffusion vector
Q	energy release from the reaction
R, r	tube radius (channel half-width in a 2D case)
R_p	universal gas constant
Sc	Schmidt number
S_L	unstretched laminar burning velocity
t	time
T	temperature
U, u	velocity
v	dimensionless axial velocity
w	dimensionless radial velocity
x, r	radial coordinate
Y	mass fraction of fuel
Z, z	axial coordinate
α	auxiliary constant
γ	adiabatic index ($\gamma = C_P/C_V$)
ε	total energy per unit volume
$\zeta_{i,j}$	stress tensor
η	dimensionless radial coordinate
Θ	gas expansion ratio ($\Theta = \rho_u/\rho_b$)

ϑ	instantaneous expansion factor
μ	dynamical viscosity
ξ	dimensionless axial coordinate
ρ	density
σ	scaled acceleration rate
τ	scaled time ($\tau = S_L t/R$)
τ_R	factor of time dimension in Arrhenius law

Subscripts

0	initial
b	burnt gas
f	flame, flame skirt
s	sidewall
sph	instant/locus when the flame shape changes from a spherical to a fingered one
tip	flame tip
u	unburnt mixture
w	wave
$wall$	flame touches side walls of tube

Other designations

\sim	scaled value
--------	--------------

1. INTRODUCTION

Spontaneous acceleration of a flamefront propagating from the closed end of a tube is a key element in deflagration-to-detonation transition (DDT) [1–5], with two main mechanisms identified as possible reasons for flame acceleration: the first is by Shelkin [6] for flames in tubes with smooth walls, and the second by Bychkov et al. [7] for flames in obstructed tubes. According to the Shelkin mechanism, flames accelerate in smooth tubes due to the non-slip boundary conditions at the walls. Quantitative theory of the process has been developed and validated by extensive numerical simulations in Refs. [8, 9]. Unlike the Shelkin mechanism, the delayed burning between the obstacles in obstructed tubes produces a powerful jet flow driving an extremely fast flame acceleration in the unobstructed, central portion part of the tube [7, 10].

In addition to these two major mechanisms, another possible scenario of flame acceleration in tubes has been demonstrated experimentally by Clanet and Searby [11]. The mechanism [11] concerns with the early stage of burning of a flame ignited at the center of the end face of a closed tube. In this configuration, an initially hemispherical flame kernel becomes eventually deformed into a finger shaped front as illustrated in Fig. 1. The tip of this finger flame experiences short but powerful acceleration until the flame skirt touches the tube walls. Thereafter, the flame acceleration stops, the flame skirt catches up with the tip quite fast and the flame becomes inverted into a “tulip” shape. Originally, the finger flame acceleration was studied in the context of the problem of “tulip flame” formation [11]. However, it was pointed out in Refs. [5, 12] that the notion of “tulip flames” is too ambiguous, since it may be attributed to any concave flame front with a cusp pointing to the burnt matter. Consequently, by mentioning “tulip flames” one may refer to numerous combustion phenomena with little or no relation to each other [13–16]. It should be noted that accelerating turbulent flames in channels with no-slip at the walls also demonstrate an irregular “tulip” flame shape [5]. To avoid the ambiguity, in the present paper we discuss only the the laminar finger flame acceleration during the initial stages of burning, without considering other manifestations of “tulip flames”. The acceleration appears to proceed in a clearly exponential regime in a number of works [11, 12, 17]. Supposedly, this is an important effect for subsequent DDT, since powerful precursor acceleration may create a leading shock wave responsible for pre-heating of the fuel mixture.

A quantitative theory of finger flame acceleration in cylindrical tubes was developed in Ref. [12] within the assumption of incompressible flow. The theory shows that, the accelerating flame tip may achieve a maximum velocity as high as $(2\Theta - 1)\Theta S_L$ at the end of the acceleration, where S_L is the planar unstretched flame speed and $\Theta \equiv \rho_u/\rho_b$ the initial ratio of the fuel mixture density to the burnt gas density. In the case of slow hydrocarbon

flames with $S_L \approx 40$ cm/s and $\Theta \approx 8$, the theory predicts the maximum velocity of the finger flame tip to be about 40 m/s, which is two orders of magnitude higher than the laminar flame speed, but it is still considerably lower than the sound speed. The situation becomes quite different for fast hydrogen-oxygen flames, with $S_L \lesssim 8$ m/s and $\Theta \approx 8$. For these values, the “incompressible” estimate of Ref. [12], $(2\Theta - 1)\Theta S_L$, yields the maximum velocity of an accelerating finger flame in the laboratory reference frame to be 960 m/s, which exceeds the sound speed in the mixture, 530 m/s, and as such fundamentally violates the incompressibility assumption. Consequently, in order to describe finger acceleration of fast flames properly, gas compressibility needs to be accounted for.

The important role of gas compressibility was discussed for flame acceleration in smooth-walled and obstructed channels. While the theoretical analysis predicts exponential flame acceleration with the incompressibility assumption flows [7–10], various experiments show moderation of the initial exponential regime with time and the possibility for the flame tip velocity to saturate to a supersonic speed in the laboratory reference frame [3, 4, 18–20]. Existence of such a saturation velocity, which correlates with the Chapman-Jouguet deflagration speed, follows from the basic theory of deflagration and detonation fronts [21, 22]. Recent numerical simulations and analytical theory demonstrate the same tendency: gas compressibility moderates the initial exponential regime of flame acceleration, modifies it to a slower one, and leads to the saturation of the flame speed [10, 24–26]. In addition, the simulations [7] have shown that in obstructed channels fast flames with a relatively high initial Mach number exhibit a noticeably lower acceleration rate as compared to slow flames. Since acceleration of finger flames has much in common with ultra-fast flame acceleration in obstructed channels [7], a similar influence of gas compressibility on the finger flame acceleration is expected.

The purpose of the present paper is to study the finger flame acceleration analytically, experimentally and computationally for various values of the unstretched laminar flame velocity, thus focusing on the influence of gas compressibility. We consider flame acceleration at the early stages of burning in tubes with slip adiabatic walls. We develop the analytical theory of flame acceleration in 2D (planar) and axisymmetric geometries through small Mach number expansion up to first-order terms. It is demonstrated that gas compression reduces the acceleration rate and moderates the finger flame acceleration noticeably. We conduct the experiments for finger flame acceleration for hydrogen-oxygen mixtures with considerably large initial values of the Mach number, which show the scaled acceleration rate to be much smaller than that obtained previously for hydrocarbon flames. We also perform numerical simulations for a wide range of initial laminar flame velocities, the results agree well with the experiments, as well as the theory in the limit of small gas compression (small initial flame velocities). Similar

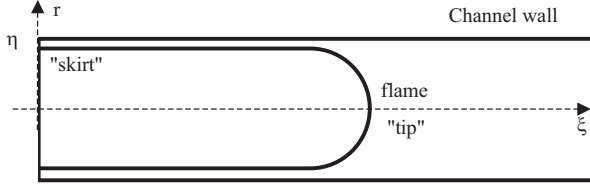


FIG. 1: Geometry of an accelerating finger flame.

to previous works, the numerical simulations show that the finger flame acceleration is followed by formation of a “tulip” flame shape, which indicates the end of the early acceleration process.

The paper consists of six technical sections. In Sections 2 A, 2 B, and 2 C we develop the theory of flame acceleration in the early stage of burning. The details of the direct numerical simulations are presented in Section 3. Section 4 A describes the experimental results; in Section 4 B we compare results from the theory, simulation and experiment, followed by the conclusions. The resolution and laminar velocity tests are presented in the Appendix.

2. THEORY OF FINGER FLAME ACCELERATION

We consider a flame front propagating in a tube/channel of radius/half-width R with an ideal slip adiabatic walls as shown in Fig. 1. One end of the tube/channel is kept closed, and the embryonic flame is ignited at the central point of the closed end wall. It was explained in Refs. [11, 12] that in the axi-symmetric, cylindrical configuration a flamefront develops from a hemi-spherical shape at the beginning to a “finger”-shape. Here we first present a 2D (planar) counterpart of this formulation, assuming flow incompressibility, and then we extend the formulation, both in the planar and axys-symmetric configurations, to the case of finite, but small compressibility.

A. Finger flame acceleration for planar geometry

In the theory we employ the standard model of an infinitely thin flame front propagating normally with the speed S_L , and use the dimensionless coordinates $(\eta, \xi) = (x, z)/R$, velocities $(w, v) = (u_x, u_z)/S_L$, and time $\tau = S_L t/R$. A 2D flame, ignited at the point $(\eta, \xi) = (0, 0)$, is initially hemi-circular, but the flame shape changes as the flame “skirt” η_f moves along the end wall of the chamber ($\xi = 0$) from the axis ($\eta = 0$) to the sidewall ($\eta = 1$), as shown in Fig. 2. The flame separates the flow into two regions of the fresh fuel mixture and the burnt gas.

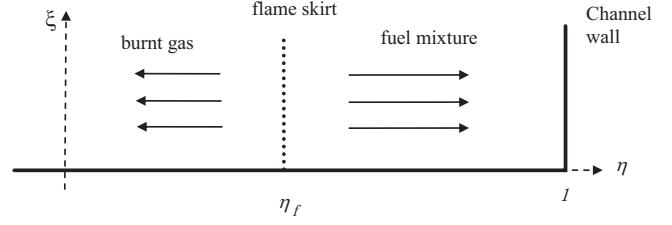


FIG. 2: Flow close to the channel wall.

Assuming incompressibility for substantially subsonic flame propagation, the continuity equation is given by

$$\frac{\partial w}{\partial \eta} + \frac{\partial v}{\partial \xi} = 0. \quad (2.1)$$

The boundary conditions are $v = 0$ at the end wall, $\xi = 0$, and $w = 0$ at the side wall, $\eta = 1$. The flow in the fresh mixture (label “u”) is assumed to be potential, so Eq. (2.1) yields

$$v_u = C_1 \xi, \quad w_u = C_1 (1 - \eta), \quad (2.2)$$

where the factor C_1 may depend on time, but is independent of the (radial) coordinate. Recognizing that while the flow in the burnt gas (label “b”) is rotational in general because of the curved flame shape, we can nevertheless treat it as a potential flow close to the end wall, where the flame front is locally planar, see Fig. 2. Subsequently, Eq. (2.1) with the boundary condition at the channel axis, $w = 0$ at $\eta = 0$, yields the velocity distribution in the burnt gas in the form

$$v_b = C_2 \xi, \quad w_b = -C_2 \eta. \quad (2.3)$$

The matching conditions at the flame front, $\eta = \eta_f$, are

$$\frac{d\eta_f}{d\tau} - w_u = 1, \quad (2.4)$$

$$v_u = v_b, \quad (2.5)$$

$$w_u - w_b = \Theta - 1. \quad (2.6)$$

Here Eq. (2.4) specifies the fixed propagation velocity S_L of the flame front with respect to the fuel mixture, while Eqs. (2.5) and (2.6) describe continuity of the tangential velocity at the front and the jump of the normal velocity, respectively. Substituting Eqs. (2.2)–(2.3) into Eqs. (2.4)–(2.6), we find $C_1 = C_2 = (\Theta - 1)$. Consequently,

$$v_u = v_b = (\Theta - 1) \xi, \\ w_u = (\Theta - 1) (1 - \eta), \quad w_b = -(\Theta - 1) \eta, \quad (2.7)$$

and the evolution equation for the flame skirt, Eq. (2.4), becomes

$$\frac{d\eta_f}{d\tau} - (\Theta - 1)(1 - \eta_f) = 1, \quad (2.8)$$

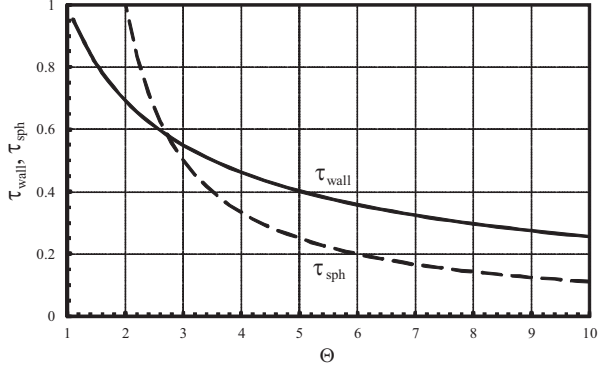


FIG. 3: Time limits of the flame acceleration.

which can be integrated with the initial condition $\eta_f = 0$ at $\tau = 0$ as

$$\eta_f = \frac{\Theta}{\Theta - 1} \{1 - \exp[-(\Theta - 1)\tau]\},$$

$$\tau = -\frac{1}{\Theta - 1} \ln \left(1 - \frac{\Theta - 1}{\Theta} \eta_f\right). \quad (2.9)$$

According to Eqs. (2.8) and (2.9), we identify two regimes of flame propagation: the regime for which the flame skirt is close to the axis, $\eta_f \ll 1$, and the one for which it is close to the wall, $1 - \eta_f \ll 1$. In the limit of $\eta_f \ll 1$ and $(\Theta - 1)\tau \ll 1$, the flame propagates as $d\eta_f/d\tau = \Theta$, $\eta_f = \Theta\tau$ (i.e. $\dot{R}_f = \Theta S_L$, $R_f = \Theta S_L t$), which is obviously related to the expansion of a hemi-circular flame front. In the other limit, of $1 - \eta_f \ll 1$, a locally planar flame “skirt” approaches the wall, the radial velocity of the fresh fuel mixture tends to zero, and the flame skirt propagates with the planar flame speed with respect to the end wall of the channel, $d\eta_f/d\tau = 1$ (i.e. $\dot{R}_f = S_L$). We can estimate the time of the transition from the hemi-circular to the “finger”-shape flame-front as

$$\tau_{sph} \approx \frac{1}{\Theta - 1}, \quad (2.10)$$

when the flame skirt position, Eq. (2.9), is $\eta_{f,sph} = (1 - e^{-1})\Theta/(\Theta - 1) \approx 0.63\Theta/(\Theta - 1)$ so the transition occurs approximately when the flame skirt has moved more than its half-way to the side wall of the channel. Substituting $\eta_f = 1$ into Eq. (2.10) we find the time instant when the flame skirt touches the tube wall

$$\tau_{wall} = \frac{\ln \Theta}{\Theta - 1}. \quad (2.11)$$

The results (2.10) and (2.11) are shown in Fig. 3 as functions of the expansion factor Θ . It is clearly seen from Eqs. (2.10) and (2.11) and Fig. 3 that the acceleration occurs ($\tau_{sph} < \tau_{wall}$) if $\Theta > e$. For $\Theta = 5 \sim 10$ we have $\tau_{sph} \approx 0.11 \sim 0.25$, while $\tau_{wall} = 0.25 \sim 0.4$.

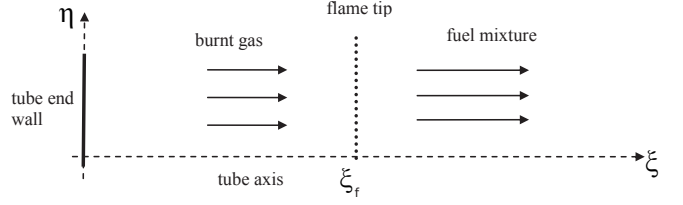


FIG. 4: Flow close to the channel axis.

To determine the evolution of the flame tip, we consider the flow along the channel axis, $\eta = 0$, as shown in Fig. 4. Based on the condition of a fixed propagation velocity of a planar flame front with respect to the burnt gas,

$$\frac{d\xi_{tip}}{d\tau} - v_b = \Theta, \quad (2.12)$$

with v_b given by Eq. (2.7), we arrive at the differential equation for the flame tip,

$$\frac{d\xi_{tip}}{d\tau} - (\Theta - 1)\xi_{tip} = \Theta, \quad (2.13)$$

with the initial condition $\xi_{tip}(0) = 0$, and the solution

$$\xi_{tip} = \frac{\Theta}{\Theta - 1} \{\exp[(\Theta - 1)\tau] - 1\}, \quad (2.14)$$

which yields a hemi-circular flame front just after ignition, $(\Theta - 1)\tau \ll 1$, when Eq. (2.14) reduces to $\xi_{tip} = \Theta\tau = \eta_f$, and the transition to the exponential acceleration thereafter. At the end of the acceleration, when the flame skirt touches the wall, we have $\tau = \tau_{wall}$, so the position of the flame tip is

$$\xi_{wall} = \xi_{tip}(\tau_{wall}) = \Theta, \quad (2.15)$$

or $Z_{wall} = \Theta R$ in dimensional units. Therefore, accounting for Eq. (2.13), we have

$$\left(\frac{d\xi_{tip}}{d\tau}\right)_{wall} = \left(\frac{u_{tip}}{S_L}\right)_{max} = \Theta^2. \quad (2.16)$$

To describe the flame shape and evaluate the total increase in the flame surface area during the flame acceleration, we note that at the end of the acceleration the flame shape is almost self-similar, with $\eta_f \approx 1$ and $\xi_{tip} \propto \exp[(\Theta - 1)\tau] \gg 1$. We therefore look for the flame shape in the form

$$\begin{aligned} \xi_f &= \xi_{tip}(\tau) - f(\tau, \eta), \\ f(\tau, \eta) &= \varphi(\eta) \exp[(\Theta - 1)\tau]. \end{aligned} \quad (2.17)$$

The accuracy of such an approximation is $\Theta^{-1} \ll 1$, which is acceptable for typical flames. Then the equation of flame evolution with respect to the burnt gas can be written as

$$\frac{\partial f}{\partial \tau} + w_b \frac{\partial f}{\partial \eta} - v_b = \Theta \left[1 + \left(\frac{\partial f}{\partial \eta}\right)^2\right]^{1/2} \approx \Theta \frac{\partial f}{\partial \eta}. \quad (2.18)$$

Accounting for the exponential state of flame acceleration, Eq. (2.17) and the velocity distribution (2.3), we reduce Eq. (2.18) to

$$[\Theta - (\Theta - 1)\eta] \frac{d\varphi}{d\eta} = \Theta, \quad (2.19)$$

with the boundary condition at the axis, $\varphi(0) = 0$, yielding the solution

$$\varphi(\eta) = -\frac{\Theta}{\Theta - 1} \ln \left(1 - \frac{\Theta - 1}{\Theta} \eta \right), \quad (2.20)$$

where

$$\xi_f(\eta, \tau) = \frac{\Theta}{\Theta - 1} \left\{ 1 - \ln \left(1 - \frac{\Theta - 1}{\Theta} \eta \right) \right\} \times \exp[(\Theta - 1)\tau] - 1. \quad (2.21)$$

Then the maximum increase in the flame length (achieved when a flame skirt touches the wall) is

$$\begin{aligned} L_w/2R &= \int_0^1 \sqrt{1 + \left(\frac{\partial f}{\partial \eta} \right)^2} d\eta \approx \int_0^1 \frac{\partial f}{\partial \eta} d\eta = f(1, \tau_{wall}) = \\ &= \varphi(1) \exp[(\Theta - 1)\tau_{wall}] = \frac{\Theta^2 \ln \Theta}{\Theta - 1}. \end{aligned} \quad (2.22)$$

B. Influence of gas compressibility on acceleration rate for planar geometry

We next consider the problem with the accuracy of the first order for the initial flame propagation Mach number $Ma \equiv S_L/c_{S,0} \ll 1$, where $c_{S,0}$ is the initial sound speed of the fresh mixture. This approach is conceptually close to that of Refs. [25, 26]. The compressible counterpart of Eq. (2.12) for the dynamics of the flame tip becomes

$$\frac{d\xi_{tip}}{d\tau} - v_{bf} = \vartheta, \quad (2.23)$$

where $v_{bf} = v_b(\xi_f, \tau)$ is the flow velocity of the burnt gas in the ξ -direction just at the flame front, and $\vartheta \equiv \rho_u/\rho_{bf}$ the instantaneous gas expansion factor, with $\vartheta_0 \equiv \Theta$.

As long as $Ma \ll 1$, we can treat the flow ahead of the flame as isentropic. In this case, to first order in Ma , we have the following relations for the scaled density $\tilde{\rho}_u = \rho_u/\rho_{u,0}$, pressure $\tilde{P}_u = P_u/P_{u,0}$, and temperature $\tilde{T}_u = T_u/T_{u,0}$ in the fuel mixture

$$\begin{aligned} \tilde{\rho}_u &= \left(1 + \frac{\gamma - 1}{2} \frac{v_u}{c_{S,0}} \right)^{\frac{2}{\gamma - 1}} \approx 1 + \frac{v_u}{c_{S,0}} \approx \\ &\approx 1 + Ma(\Theta - 1)(\xi_{tip} + 1), \end{aligned} \quad (2.24)$$

$$\begin{aligned} \tilde{P}_u &= \left(1 + \frac{\gamma - 1}{2} \frac{v_u}{c_{S,0}} \right)^{\frac{2\gamma}{\gamma - 1}} \approx 1 + \gamma \frac{v_u}{c_{S,0}} \approx \\ &\approx 1 + Ma\gamma(\Theta - 1)(\xi_{tip} + 1), \end{aligned} \quad (2.25)$$

$$\begin{aligned} \tilde{T}_u &= \left(1 + \frac{\gamma - 1}{2} \frac{v_u}{c_{S,0}} \right)^2 \approx 1 + (\gamma - 1) \frac{v_u}{c_{S,0}} \approx \\ &\approx 1 + Ma(\gamma - 1)(\Theta - 1)(\xi_{tip} + 1), \end{aligned} \quad (2.26)$$

where $\gamma \equiv C_P/C_V$ is the adiabatic index. It is noted that Eqs. (2.24)–(2.26) also define the rigorous mathematical limit of validity for the present theory, i.e. $v_u/c_{S,0} \ll 1$. The matching relations at the flame front are

$$\tilde{\rho}_u \left(\frac{d\xi_{tip}}{d\tau} - v_u \right) = \tilde{\rho}_{bf} \left(\frac{d\xi_{tip}}{d\tau} - v_{bf} \right), \quad (2.27)$$

$$\tilde{P}_u + \tilde{\rho}_u \left(\frac{d\xi_{tip}}{d\tau} - v_u \right)^2 = \tilde{P}_{bf} + \tilde{\rho}_{bf} \left(\frac{d\xi_{tip}}{d\tau} - v_{bf} \right)^2, \quad (2.28)$$

$$\begin{aligned} \tilde{T}_u + \tilde{Q} + \frac{1}{2C_P T_{u,0}} \left(\frac{d\xi_{tip}}{d\tau} - v_u \right)^2 &= \\ = \tilde{T}_{bf} + \frac{1}{2C_P T_{u,0}} \left(\frac{d\xi_{tip}}{d\tau} - v_{bf} \right)^2, \end{aligned} \quad (2.29)$$

where $\tilde{Q} \equiv Q/C_P T_{u,0} = \Theta - 1$ is the scaled reaction heat release. With the first-order approximation for small Ma , we reduce Eqs. (2.28) and (2.29) to

$$\tilde{P}_u = \tilde{P}_{bf}, \quad \tilde{T}_u + \Theta - 1 = \tilde{T}_{bf}. \quad (2.30)$$

Using subsequently the perfect gas law, $\tilde{\rho}_u \tilde{T}_u = \tilde{\rho}_{bf} \tilde{T}_{bf}$, as well as Eq. (2.26), we find

$$\vartheta = 1 + \frac{\Theta - 1}{\tilde{T}_u} = \Theta - Ma(\gamma - 1)(\Theta - 1)^2(\xi_{tip} + 1). \quad (2.31)$$

While, according to the Euler equation

$$\frac{\partial v_b}{\partial \tau} + v_b \frac{\partial v_b}{\partial \xi} = -\frac{1}{\tilde{\rho}_b} \frac{\partial \tilde{P}_b}{\partial \xi}, \quad (2.32)$$

pressure is uniform in the burnt gas, $\tilde{P}_b(t) = \tilde{P}_{bf}$, up to the first-order in $Ma \ll 1$, it however grows in time, and thereby increases the temperature and density of the burnt gas due to adiabatic compression.

Now we shall consider propagation of a nearly planar flame “skirt”. Within the accuracy of Ma , the pressure in fuel mixture between the flame front and the sidewall is the same as that in the burnt gas, $\tilde{P}_s = \tilde{P}_b(\tau) = \tilde{P}_{bf} = \tilde{P}_u$. Thus the density and temperature of the fuel mixture around the flame skirt are the same as those of the fuel mixture just ahead of the flame tip, since in both cases we have adiabatic compression and the same final pressure. Consequently, the continuity equation for the fuel in the domain between the flame skirt and the side wall, $\eta_f < \eta < 1$, takes the form

$$\frac{\partial w_s}{\partial \eta} \approx -\frac{1}{\tilde{\rho}_s} \frac{d\tilde{\rho}_s}{d\tau} = -\frac{1}{\gamma \tilde{P}_s} \frac{d\tilde{P}_s}{d\tau} = -\frac{1}{\gamma \tilde{P}_u} \frac{d\tilde{P}_u}{d\tau}, \quad (2.33)$$

with the following solution satisfying the matching relation at the sidewall, $\eta = 1$, $w_s = 0$,

$$w_s = \frac{1}{\gamma \tilde{P}_u} \frac{d\tilde{P}_u}{d\tau} (1 - \eta), \quad w_{s,f} = \frac{1}{\gamma \tilde{P}_u} \frac{d\tilde{P}_u}{d\tau} (1 - \eta_f). \quad (2.34)$$

Here the subscript "s, f" designates the flow velocity just ahead of the flame skirt. Using the matching relations at the flame front, we find the velocity in the burnt gas at the flame skirt, subscripted by "s, b, f", as

$$w_{s,b,f} = w_{s,f} - \vartheta + 1 = \frac{1}{\gamma \tilde{P}_u} \frac{d\tilde{P}_u}{d\tau} (1 - \eta_f) - \vartheta + 1. \quad (2.35)$$

We subsequently solve the continuity equation, equivalent to Eq. (2.33), in the burnt gas with Eq. (2.35) to find

$$\begin{aligned} w_b &= \frac{1}{\gamma \tilde{P}_u} \frac{d\tilde{P}_u}{d\tau} (1 - \eta_f) - \vartheta + 1 + \frac{1}{\gamma \tilde{P}_u} \frac{d\tilde{P}_u}{d\tau} (\eta_f - \eta) = \\ &= \frac{1}{\gamma \tilde{P}_u} \frac{d\tilde{P}_u}{d\tau} (1 - \eta) - \vartheta + 1. \end{aligned} \quad (2.36)$$

Similarly, the continuity equation for the burnt gas around the symmetry axis takes the form

$$\frac{\partial w_b}{\partial \eta} + \frac{\partial v_b}{\partial \xi} = -\frac{1}{\gamma \tilde{P}_u} \frac{d\tilde{P}_u}{d\tau}, \quad (2.37)$$

which can be integrated as

$$v_b = (\vartheta - 1) \xi - \frac{1}{\gamma \tilde{P}_u} \frac{d\tilde{P}_u}{d\tau} \xi, \quad w_b = -(\vartheta - 1) \eta. \quad (2.38)$$

Consequently, the evolution equation for the flame tip, Eq. (2.23), becomes

$$\frac{d\xi_{tip}}{d\tau} = \left(\vartheta - 1 - \frac{1}{\gamma \tilde{P}_u} \frac{d\tilde{P}_u}{d\tau} \right) \xi_{tip} + \vartheta. \quad (2.39)$$

Finally, substituting Eqs. (2.25) and (2.31) into Eq. (2.39), omitting the second- and higher-order terms in Ma , and accounting for the zeroth-order approximation, Eq. (2.14), we obtain the equation

$$\frac{d\xi_{tip}}{d\tau} = -Ma\gamma(\Theta - 1)^2 \xi_{tip}^2 + \sigma_1 \xi_{tip} + \Theta_1, \quad (2.40)$$

with

$$\sigma_1 = (\Theta - 1) [1 - Ma(\Theta + 2(\gamma - 1)(\Theta - 1))], \quad (2.41)$$

$$\Theta_1 = \Theta - Ma(\gamma - 1)(\Theta - 1)^2. \quad (2.42)$$

In the limit of incompressible flow, $Ma = 0$, we have $\sigma_1 = \Theta - 1$, $\Theta_1 = \Theta$, and Eq. (2.40) fully reproduces Eq. (2.13). Accounting for gas compressibility, we obtain moderation of the flame acceleration in Eq. (2.40), which is provided by two types of terms: linear and nonlinear

with respect to ξ_{tip} . The linear term does not change the exponential state of the flame acceleration, though they reduce the acceleration rate to σ_1 as compared to $\Theta - 1$ for the incompressible flow. At the very beginning, for $\xi_{tip} \rightarrow 0$, the flame acceleration is moderated by the linear term only, and Eq. (2.40) reduces to

$$\frac{d\xi_{tip}}{d\tau} = \sigma_1 \xi_{tip} + \Theta_1, \quad (2.43)$$

with the solution

$$\xi_{tip} = \frac{\Theta_1}{\sigma_1} [\exp(\sigma_1 \tau) - 1]. \quad (2.44)$$

The nonlinear term of Eq. (2.40), however, becomes important quite fast and modifies the exponential state of flame acceleration to a slower one. The complete analytical solution to Eq. (2.40) is given by

$$\xi_{tip} = \frac{2\Theta_1 [\exp(\sigma_2 \tau) - 1]}{(\sigma_2 - \sigma_1) \exp(\sigma_2 \tau) + (\sigma_2 + \sigma_1)}, \quad (2.45)$$

where $\sigma_2 \equiv \sqrt{\sigma_1^2 + 4Ma\gamma\Theta_1(\Theta - 1)^2}$.

C. Influence of gas compressibility on acceleration rate for the axis-symmetric geometry

Now we reconsider the problem of finger flame propagation in an axis-symmetric, cylindrical tube, Ref. [12], incorporating compressibility with the accuracy of the first order for flame propagation Mach number.

First, we briefly recall the incompressible theory in this configuration; see Ref. [12] for details. The incompressible continuity equation in the axis-symmetric geometry takes the form

$$\frac{1}{\eta} \frac{\partial}{\partial \eta} (\eta w) + \frac{\partial v}{\partial \xi} = 0, \quad (2.46)$$

and the axis-symmetric counterparts for the velocity distributions, Eq. (2.7), and the evolution of the flame skirt, Eqs. (2.8)–(2.9), are given by

$$\begin{aligned} v_u &= v_b = 2(\Theta - 1) \eta_f \xi, \\ w_u &= (\Theta - 1) \eta_f \left(\frac{1}{\eta} - \eta \right), \\ w_b &= -(\Theta - 1) \eta_f \eta, \end{aligned} \quad (2.47)$$

$$\frac{d\eta_f}{d\tau} - (\Theta - 1)(1 - \eta_f^2) = 1 \quad \Rightarrow \quad (2.48)$$

$$\begin{aligned} \eta_f &= \frac{\Theta}{\alpha} \tanh(\alpha \tau), \\ \tau_{wall} &= \frac{1}{2\alpha} \ln \left(\frac{\Theta + \alpha}{\Theta - \alpha} \right), \\ \tau_{sph} &= \frac{1}{2\alpha}, \end{aligned} \quad (2.49)$$

where

$$\alpha = \sqrt{\Theta(\Theta - 1)}. \quad (2.50)$$

It can be readily found from Eq. (2.49) that the acceleration is possible (i.e. $\tau_{sph} < \tau_{wall}$) if $\Theta > (1 - [(e - 1)/e + 1])^2)^{-1} \approx 1.27$. For $\Theta = 5 \sim 10$, Eq. (2.49) yields $\tau_{sph} \approx 0.05 \sim 0.11$, and $\tau_{wall} \approx 0.19 \sim 0.32$. These quantities are much smaller than those for the planar geometry, Eqs. (2.10) and (2.11), making an indirect proof that for the axisymmetric geometry acceleration proceeds faster than for the planar one.

With the result (2.47), the equation for the flame tip, $\xi_{tip} - v_b = \Theta$, becomes

$$\frac{d\xi_{tip}}{d\tau} - 2(\Theta - 1)\eta_f(\tau)\xi_{tip}(\tau) = \Theta, \quad (2.51)$$

or

$$\frac{d\xi_{tip}}{d\tau} - 2\alpha \tanh(\alpha\tau)\xi_{tip} = \Theta, \quad (2.52)$$

with the solution

$$\xi_{tip} = \frac{\Theta}{2\alpha} \sinh(2\alpha\tau), \quad (2.53)$$

which also yields $\xi_{wall} = \Theta$ similar to the 2D result (2.15). At sufficiently late time instants we have $\eta_f \approx 1$ and Eqs. (2.51)–(2.52) reduce to

$$\begin{aligned} \frac{d\xi_{tip}}{d\tau} &= 2\alpha\xi_{tip} + \Theta \implies \\ \xi_{tip} &= \frac{\Theta}{2\alpha} [\exp(2\alpha\tau) - 1], \end{aligned} \quad (2.54)$$

so the flame tip accelerates almost exponentially, with the acceleration rate $\sigma_0 = 2\alpha = 2\sqrt{\Theta(\Theta - 1)}$. This result exceeds considerably (by a factor of about 2) its 2D counterpart $(\Theta - 1)$ in Eq. (2.14); and it is a little less than the model estimation 2Θ of Clanet and Searby [11].

Now we shall account for small, but finite gas compression. With the axial velocity v_u given by Eq. (2.47), the axisymmetric counterparts of Eqs. (2.24)–(2.26) and (2.31) take the form

$$\begin{aligned} \tilde{\rho}_u &= \left(1 + \frac{\gamma - 1}{2} \frac{v_u}{c_0}\right)^{\frac{2}{\gamma - 1}} \\ &\approx 1 + Ma(2\alpha\xi_{tip} + \Theta - 1), \end{aligned} \quad (2.55)$$

$$\begin{aligned} \tilde{P}_u &= \left(1 + \frac{\gamma - 1}{2} \frac{v_u}{c_0}\right)^{\frac{2\gamma}{\gamma - 1}} \\ &\approx 1 + Ma\gamma(2\alpha\xi_{tip} + \Theta - 1), \end{aligned} \quad (2.56)$$

$$\begin{aligned} \tilde{T}_u &= \left(1 + \frac{\gamma - 1}{2} \frac{v_u}{c_0}\right)^2 \\ &\approx 1 + Ma(\gamma - 1)(2\alpha\xi_{tip} + \Theta - 1), \end{aligned} \quad (2.57)$$

$$\vartheta = \Theta - Ma(\gamma - 1)(\Theta - 1)^2 \left(2\frac{\Theta}{\alpha}\xi_{tip} + 1\right). \quad (2.58)$$

Following the strategy of Section 2 B, we find

$$\frac{1}{\eta} \frac{\partial}{\partial \eta} (\eta w_b) + \frac{\partial v_b}{\partial \xi} = -\frac{1}{\gamma \tilde{P}_u} \frac{d\tilde{P}_u}{d\tau} \implies \quad (2.59)$$

$$v_b = 2(\vartheta - 1)\eta_f\xi - \frac{1}{\gamma \tilde{P}_u} \frac{d\tilde{P}_u}{d\tau}\xi, \quad w_b = -(\vartheta - 1)\eta_f\eta. \quad (2.60)$$

Similar to Eqs. (2.48) and (2.49), the flame skirt position is given by

$$\frac{d\eta_f}{d\tau} - (\vartheta - 1)(1 - \eta_f^2) = 1 \implies \eta_f = \frac{\vartheta}{\hat{\alpha}} \tanh(\hat{\alpha}\tau), \quad (2.61)$$

where $\hat{\alpha} = \sqrt{\vartheta(\vartheta - 1)}$, and the evolution equation for the flame tip takes the form

$$\frac{d\xi_{tip}}{d\tau} = \left(2(\vartheta - 1)\eta_f - \frac{1}{\gamma \tilde{P}_u} \frac{d\tilde{P}_u}{d\tau}\right)\xi_{tip} + \vartheta. \quad (2.62)$$

Holding the zeroth- and first-order approximation for Ma in the terms of Eq. (2.62), we rewrite it in the form

$$\begin{aligned} \frac{d\xi_{tip}}{d\tau} &= [2\hat{\alpha} \tanh(\hat{\alpha}\tau) - 2Ma\vartheta\alpha]\xi_{tip} - \\ &- 4Ma\alpha\hat{\alpha} \tanh(\hat{\alpha}\tau)\xi_{tip}^2 + \vartheta, \end{aligned} \quad (2.63)$$

or

$$\begin{aligned} \frac{d\xi_{tip}}{d\tau} &= \{2\alpha_1 \tanh(\alpha_1\tau) - 2Ma\alpha[1 + \gamma(\Theta - 1)]\}\xi_{tip} - \\ &- 2Ma\left\{\frac{\alpha\tau B}{\cosh^2(\alpha\tau)} + (2\alpha^2 - B) \tanh(\alpha\tau)\right\}\xi_{tip}^2 + \\ &+ \Theta_1 \end{aligned} \quad (2.64)$$

where Θ_1 is the same as in the planar geometry, Eq. (2.42),

$$\Theta_1 = \Theta - Ma(\gamma - 1)(\Theta - 1)^2, \quad (2.65)$$

and

$$\alpha_1 = \sqrt{\Theta_1(\Theta_1 - 1)}, \quad B = (\gamma - 1)(\Theta - 1)(2\Theta - 1). \quad (2.66)$$

In general, Eq. (2.64) has to be solved computationally, but we shall integrate it analytically within several asymptotical approaches. First of all, in the limit of $Ma = 0$, we have $\Theta_1 = \Theta$, $\alpha_1 = \alpha$ and Eq. (2.64) reproduces Eq. (2.52). Even for finite gas compressibility, the effect of the nonlinear term in Eq. (2.64) is negligible in the very beginning, hence Eq. (2.64) can be approximated by

$$\frac{d\xi_{tip}}{d\tau} = \{2\alpha_1 \tanh(\alpha_1\tau) - 2Ma\alpha[1 + \gamma(\Theta - 1)]\}\xi_{tip} + \Theta_1, \quad (2.67)$$

with the solution to the first order approximation for Ma

$$\begin{aligned} \xi_{tip} &= \frac{\Theta_1}{2\alpha_1} \sinh(2\alpha_1\tau) - \\ &- 2Ma \frac{\Theta}{\alpha} [1 + \gamma(\Theta - 1)] \cosh^2(\alpha\tau) \ln \cosh(\alpha\tau). \end{aligned} \quad (2.68)$$

The nonlinear term of Eq. (2.64), however, becomes important quite fast, modifying the state of flame acceleration to a slower one, and hence making the asymptote (2.68) incorrect. However, at a sufficiently late stage of the acceleration, we can estimate $\tanh(\alpha_1\tau) \sim 1$, hence $\eta_f \sim \vartheta/\hat{\alpha}$, and Eq. (2.64) is reduced to for similar to that of the 2D Eq. (2.40),

$$\frac{d\xi_{tip}}{d\tau} = -Ma\psi\xi_{tip}^2 + \sigma_1\xi_{tip} + \Theta_1, \quad (2.69)$$

where

$$\psi = 2(\Theta - 1)(2\Theta\gamma - \gamma + 1), \quad (2.70)$$

$$\sigma_1 = \sigma_0 \left\{ 1 - Ma \left[\Theta + \left(2 - \frac{1}{2\Theta} \right) (\gamma - 1)(\Theta - 1) \right] \right\}, \quad (2.71)$$

and with the solution, Eq. (2.45),

$$\xi_{tip} = \frac{2\Theta_1[\exp(\sigma_2\tau) - 1]}{(\sigma_2 - \sigma_1)\exp(\sigma_2\tau) + (\sigma_2 + \sigma_1)}, \quad (2.72)$$

where $\sigma_2 \equiv \sqrt{\sigma_1^2 + 4\Theta_1 Ma\psi}$. Obviously, the result (2.69), (2.72) fully recovers the properties of its planar counterpart: in the limit of $Ma = 0$ we have $\sigma_1 = \sigma_0$, and Eqs. (2.69) and (2.72) reduce to Eq. (2.54); accounting for gas compressibility, we obtain linear and nonlinear moderation of the flame acceleration with respect to ξ_{tip} . Reducing the acceleration rate from σ_0 to σ_1 , the linear terms do not change the exponential state of acceleration while the nonlinear term of Eq. (2.69) modifies the exponential state of flame acceleration to a slower one as soon as it becomes important.

It is emphasized that the result (2.72) does not reproduce the asymptote (2.68) as they are related to opposite limiting cases. Consequently, it is expected that for certain range of Ma the complete (numerical) solution to Eq. (2.64) lies in between the two values given by Eqs. (2.68) and (2.72).

3. NUMERICAL METHOD, BASIC EQUATIONS, BOUNDARY AND INITIAL CONDITIONS

We perform direct numerical simulations of the hydrodynamic and combustion equations including transport processes (thermal conduction, diffusion, viscosity) and chemical kinetics in the form of Arrhenius equation. Both 2D planar and axisymmetric cylindrical flows are investigated. In the general tensor form the governing equations read

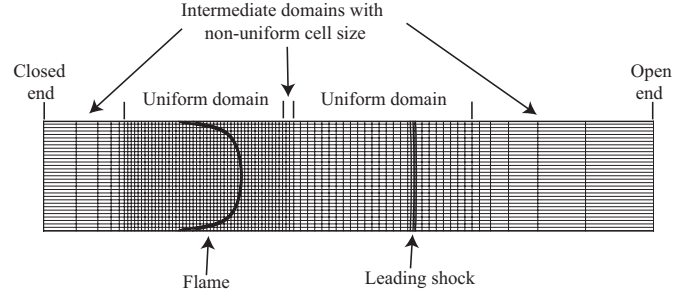


FIG. 5: The sketch of the grid with variable resolution used in numerical simulations.

$$\frac{\partial \rho}{\partial t} + \frac{1}{r^\beta} \frac{\partial}{\partial r} (r^\beta \rho u_r) + \frac{\partial}{\partial z} (\rho u_z) = 0, \quad (3.1)$$

$$\begin{aligned} \frac{\partial}{\partial t} (\rho u_r) + \frac{1}{r^\beta} \frac{\partial}{\partial r} [r^\beta (\rho u_r^2 - \zeta_{r,r})] + \\ + \frac{\partial}{\partial z} (\rho u_r u_z - \zeta_{r,z}) + \frac{\partial P}{\partial r} + \psi_\beta = 0, \end{aligned} \quad (3.2)$$

$$\begin{aligned} \frac{\partial}{\partial t} (\rho u_z) + \frac{1}{r^\beta} \frac{\partial}{\partial r} [r^\beta (\rho u_r u_z - \zeta_{r,z})] + \\ + \frac{\partial}{\partial z} (\rho u_z^2 - \zeta_{z,z}) + \frac{\partial P}{\partial z} = 0, \end{aligned} \quad (3.3)$$

$$\begin{aligned} \frac{\partial \varepsilon}{\partial t} + \frac{1}{r^\beta} \frac{\partial}{\partial r} [r^\beta ((\varepsilon + P) u_r - \zeta_{r,r} u_r - \zeta_{r,z} u_z + q_r)] + \\ + \frac{\partial}{\partial z} [(\varepsilon + P) u_z - \zeta_{z,z} u_z - \zeta_{r,z} u_r + q_z] = 0, \end{aligned} \quad (3.4)$$

$$\begin{aligned} \frac{\partial}{\partial t} (\rho Y) + \frac{1}{r^\gamma} \frac{\partial}{\partial r} \left[r^\gamma \left(\rho u_r Y - \frac{\mu}{Sc} \frac{\partial Y}{\partial r} \right) \right] + \\ + \frac{\partial}{\partial z} \left(\rho u_z Y - \frac{\mu}{Sc} \frac{\partial Y}{\partial z} \right) = \\ = -\frac{\rho Y}{\tau_R} \exp(-E_a/R_p T), \end{aligned} \quad (3.5)$$

where $\beta = 0$ and 1 for 2D and axisymmetric geometries, respectively,

$$\varepsilon = \rho(QY + C_V T) + \frac{\rho}{2} (u_z^2 + u_r^2) \quad (3.6)$$

is the total energy per unit volume, Y the mass fraction of the fuel, Q the reaction energy release from the reaction, and C_V the heat capacity at constant volume. The energy diffusion vector q_i is given by

$$q_r = -\mu \left(\frac{C_P}{Pr} \frac{\partial T}{\partial r} + \frac{Q}{Sc} \frac{\partial Y}{\partial r} \right), \quad (3.7)$$

$$q_z = -\mu \left(\frac{C_P}{Pr} \frac{\partial T}{\partial z} + \frac{Q}{Sc} \frac{\partial Y}{\partial z} \right). \quad (3.8)$$

The stress tensor $\zeta_{i,j}$ takes the form

$$\zeta_{i,j} = \mu \left(\frac{\partial u_i}{\partial x_j} + \frac{\partial u_j}{\partial x_i} - \frac{2}{3} \frac{\partial u_k}{\partial x_k} \delta_{i,j} \right) \quad (3.9)$$

in the 2D configuration ($\beta = 0$), while in the axisymmetric geometry ($\beta = 1$) it reads

$$\zeta_{r,r} = \frac{2\mu}{3} \left(2 \frac{\partial u_r}{\partial r} - \frac{\partial u_z}{\partial z} - \frac{u_r}{r} \right), \quad (3.10)$$

$$\zeta_{z,z} = \frac{2\mu}{3} \left(2 \frac{\partial u_z}{\partial z} - \frac{\partial u_r}{\partial r} - \frac{u_r}{r} \right), \quad (3.11)$$

$$\zeta_{r,z} = \mu \left(\frac{\partial u_r}{\partial z} + \frac{\partial u_z}{\partial r} \right). \quad (3.12)$$

Finally, the last term in Eq. (3.2) takes the form

$$\psi_\beta = \frac{2\mu}{3} \left(2 \frac{u_r}{r} - \frac{\partial u_r}{\partial r} - \frac{\partial u_z}{\partial z} \right) \quad (3.13)$$

if $\beta = 1$, and $\psi_\beta = 0$ if $\beta = 0$. Here μ is the dynamic viscosity, and Pr and Sc the Prandtl and Schmidt numbers, respectively.

We take unity Lewis number $Le \equiv \text{Sc}/\text{Pr} = 1$, with $\text{Pr} = \text{Sc} = 0.75$; the dynamical viscosity is $\mu = 1.7 \times 10^{-5} \text{Ns/m}^2$. The fuel-air mixture and burnt gas are perfect gases with a constant molar mass $m = 2.9 \times 10^{-2} \text{kg/mol}$, with $C_V = 5R_p/2m$, $C_P = 7R_p/2m$, and the equation of state

$$P = \rho R_p T / m, \quad (3.14)$$

where $R_p \approx 8.31 \text{J}/(\text{mol} \cdot \text{K})$ is the universal gas constant. We consider a single-step irreversible reaction of the first order with the temperature dependence of the reaction rate given by the Arrhenius law with an activation energy E_a and the factor of time dimension τ_R . In our simulations we took $E_a/R_p T_u = 32$ in order to have better resolution of the reaction zone. The factor τ_R was adjusted to obtain a particular value of the planar flame velocity S_L by solving the associated eigenvalue problem. The flame thickness is defined as

$$L_f \equiv \frac{\mu_u}{\text{Pr} \rho_u S_L}, \quad (3.15)$$

where $\rho_u = 1.16 \text{kg/m}^3$ is the unburned mixture density. It is noted that L_f is just a mathematical parameter of length dimension related to the flame front, while the real effective diffusion flame thickness is considerably larger [28, 29]. We take initial temperature of the fuel mixture $T_{u,0} = 300 \text{K}$, initial pressure $P_{u,0} = 10^5 \text{Pa}$, specific heat ratio $\gamma = 1.4$, and initial density ratio of the fuel mixture and the burnt gas $\Theta = \rho_u/\rho_b = 8$. We perform the simulations for a rather wide range of initial Mach number $Ma = S_L/c_{S,0} = 10^{-3} \sim 1.6 \times 10^{-2}$. Lower value of the Mach number are relevant for hydrocarbon

flames, while higher values for hydrogen-oxygen flames [20]. We use the tube diameter $2R = 150L_f$ for axisymmetric simulations and channel width $2R = 100L_f$ for 2D simulations.

Similar to the theoretical assumptions, we adopt slip and adiabatic boundary conditions at the tube walls:

$$\mathbf{n} \cdot \mathbf{u} = 0, \quad \mathbf{n} \cdot \nabla T = 0, \quad (3.16)$$

where \mathbf{n} is the unit normal vector at the walls. At the end of the open tube/channel non-reflecting boundary conditions are applied. As initial conditions, we used a hemi-spherical (hemi-circular) flame “ignited” at the channel axis at the closed end of the tube, with its structure given by the analytical solution of Zel’dovich and Frank-Kamenetskii [1, 2]

$$T = T_u + (T_b - T_u) \exp \left(-\sqrt{x^2 + z^2}/L_f \right), \quad \text{if } z^2 + x^2 < r_f^2 \quad (3.17)$$

$$T = \Theta T_u, \quad \text{if } z^2 + x^2 > r_f^2 \quad (3.18)$$

$$Y = (T_b - T)/(T_b - T_f), \quad P = P_u, \quad u_x = 0, \quad u_z = 0. \quad (3.19)$$

Here r_f is the radius of the initial flame ball at the closed end of the tube. The finite initial radius of the flame ball is equivalent to a time shift, which required proper adjustments when comparing the theory and numerical simulations.

In our simulations, we used a 2D hydrodynamic Navier-Stokes code adapted for parallel computations [31]. The numerical scheme is second order accurate in time and fourth order in space for convective terms, and second order in space for diffusive terms. The code is robust and accurate; it was successfully used in aero-acoustic applications. In the present paper we performed 2D and axisymmetric simulations to save computational time and to be able to perform a large number of simulation runs required for a thorough investigation of the problem of compressibility effect on the finger flame behaviour. We used mesh with variable resolution in order to take into account the growing distances between the tube end, the accelerating flame and the pressure wave, and to resolve both chemical and hydrodynamic spatial scales. Typical computation time for one simulation required up to 10^4 CPU-hours, hence implying the need for extensive parallel calculations.

We used a rectangular grid with the grid walls parallel to the coordinate axes. The sketch of the calculation mesh used in simulations of flame acceleration from the closed tube end is shown in Fig. 5. To perform all the calculations in a reasonable time, we made the grid spacing non-uniform along the z -axis with the zones of fine grid around the flame and leading shock fronts. For majority of the simulation runs, the grid size in z -direction was $0.25L_f$ and $0.5L_f$ in the domains of the flame and shock wave, respectively, which allowed resolution of the internal structure of the flame and shock waves. Outside

P , bar	Θ	L_T , mm	C	S_L , m/s	$S_{L,C}$, m/s	Ma	Ma_C	σ_1	$\sigma_{1,C}$
0.20	8.00	2.0	0.778	6.855	5.33	0.0128	0.0100	4.18	5.373
0.60	8.260	0.5	0.944	8.395	7.928	0.0157	0.0149	4.83	5.138
0.75	8.317	0.379	0.958	8.700	8.335	0.0162	0.0157	4.90	5.110
0.75	8.317	0.379	0.958	8.700	8.335	0.0162	0.0157	5.43	5.660

TABLE I: Experiment parameters and $\sigma_{1,C}$ obtained by fitting of the results of Fig. 7 for different pressures.

the region of fine grid the mesh size increased gradually with 2% change in size between the neighboring cells. In order to keep the flame and shock waves in the zone of fine grid we implemented the periodical mesh reconstruction during the simulation run [30]. Third-order splines were used for re-interpolation of the flow variables during periodic grid reconstruction to preserve the second order accuracy of the numerical scheme.

4. RESULTS AND DISCUSSION

A. Experimental results

Experiments were performed in a channel with rectangular cross-section (50×50 mm), 6.05 m long with 24 transparent ports for photo-gauges. A high-speed schlieren system with stroboscopic pulse generator and high speed camera, germanium photodiodes and piezo-electric transducers were used to record the flame evolution. The experimental facilities are described in detail in Ref. [20] and the references given therein.

The experiments were conducted with the fast-burning, stoichiometric hydrogen-oxygen mixture at initial pressures of $0.2 \sim 0.75$ bar. The mixture was prepared by precise partial pressure method with a deviation less than $\pm 0.2\%$ with respect to H_2 fraction. By changing the initial pressure we vary the value of S_L and the initial flame Mach number. Initial ambient gas mixture temperature was $T_0 = 293K$; and the corresponding sound speed in the fresh fuel mixture is 531 m/s. The initial density ratio of the fresh fuel and burnt products are in the range $\Theta = 8.0 \sim 8.317$, depending on the initial pressure.

Fig. 6 shows the schlieren images of “finger” flame propagation at pressure 0.2 bar. It was observed that the flame tip accelerates exponentially at the initial stage of flame propagation, in agreement with previous experiments [11] and theory [12]. For the stoichiometric H_2/O_2 fuel mixture used in the present experiment the influences of diffusional-thermal cellular and pulsating instabilities [2] are ruled out. The influence of hydrodynamic Darrieus-Landau instability is negligible as well due to the strong flame curvature observed in the experiment, leading to the Zeldovich-type stabilization of the flame front perturbations [27]. Thus, in the present experiment the flame front acceleration could be attributed purely to the “finger”-flame mechanism of exponential acceleration [11, 12].

The experimentally obtained evolution of the scaled flame tip position for various pressures is shown in Fig. 7. The definition of laminar burned velocity $S_{L,C}$ used in the present scaling is described further. When the flame skirt approaches the wall, the flame acceleration moderates, and flame shape undergoes transition from a convex “finger” to a concave “tulip” shape. The instant when the flame skirt approaches the channel wall is clearly correlated with the instant at which the exponential flame tip acceleration terminates, which can be seen at Fig. 7.

Physical parameters of the experiments, as well as the scaled acceleration rates obtained from fitting of experimental results of Fig. 7 for different pressures, and the initial Mach numbers are given in Table I. The unstretched laminar flame velocity S_L and thermal flame thickness L_T are obtained from numerical simulation of one-dimensional premixed flame structure employing PREMIX code of CHEMKIN family [32] with the use of updated chemical kinetics mechanism for hydrogen oxidation [33]. The thermal flame thickness L_T is conventionally defined as [2] $(T_b - T_u)/\max(|\partial T/\partial x|)$, where T_b and T_u are the temperatures of burnt and unburnt gases, respectively, and $\max(|\partial T/\partial x|)$ is the maximum of temperature gradient. It should be noted that for low-pressure stoichiometric hydrogen-oxygen finger flames a non-negligible pure curvature effect [2] is observed in our case, therefore we introduce relevant modifications to S_L and Ma , denoted as $S_{L,C}$ and Ma_C , in such a manner that the correction parameter C is defined as $C = S_{L,C}/S_L$, so that the estimation for the corrected growth rate is given by $\sigma_{1,C} = \sigma_1/C$. The lower is the pressure (and the bigger is thermal flame thickness), the more pronounced is the pure curvature effect.

The pure curvature correction parameter C and $S_{L,C}$ and $\sigma_{1,C}$ are estimated as follows. Based on the observation from the experiments, we employ the assumption that the curvature of the flame tip remains almost constant during the time interval $\tau_{sph} < \tau < \tau_{wall}$, with τ_{sph} and τ_{wall} given by Eqs. (2.10) and (2.11), respectively. So within this time interval the flame tip radius can be approximated as

$$R_{tip} = R\eta_{f,sph} = 0.63 R\Theta/(\Theta - 1) \approx 0.72R, \quad (4.1)$$

where R is the channel half-width. Consequently, with the curvature term in the form $\nabla \cdot \mathbf{n} = 2/R_{tip}$, the curvature-modified laminar burning velocity at the flame

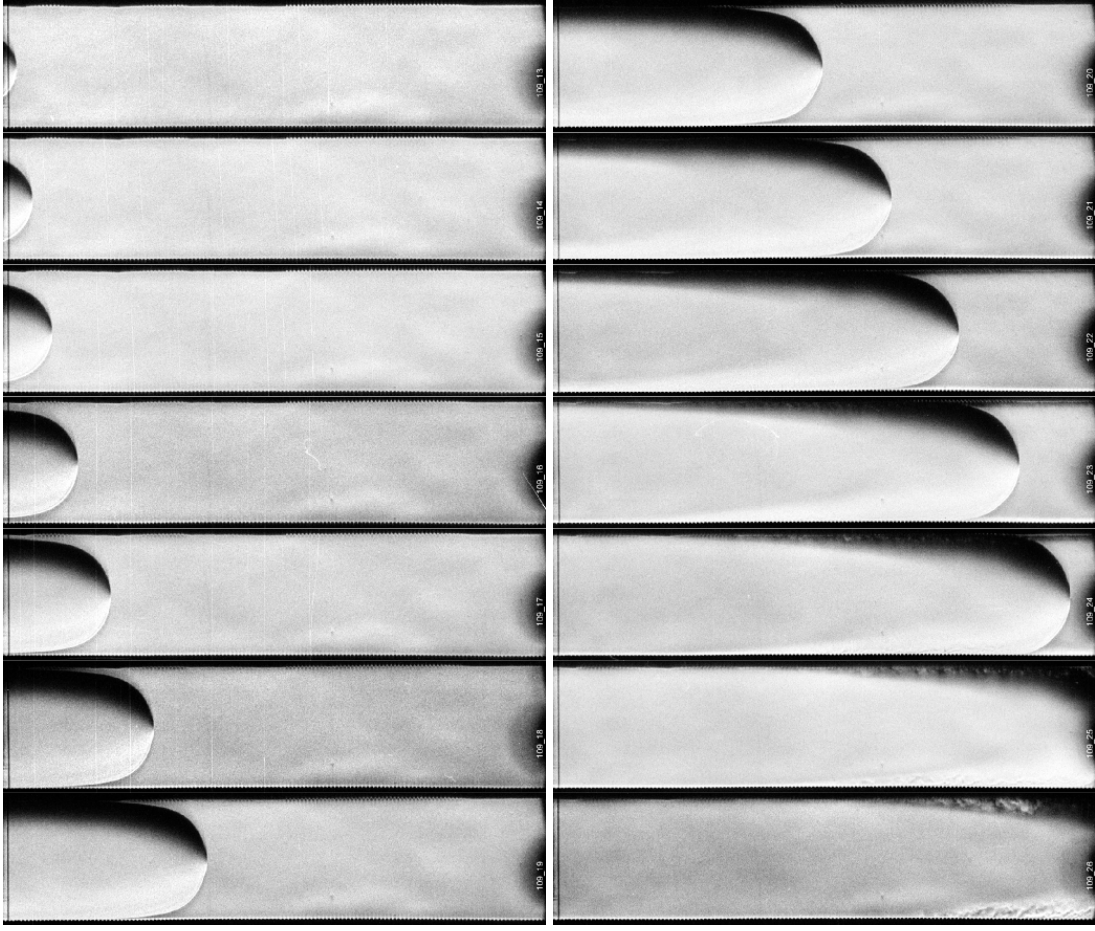


FIG. 6: Schlieren images of finger flame propagation for stoichiometric H_2/O_2 mixture at pressure 0.2 bar. The shown images are evenly distributed in time with interval of 100 ms. Note that the shift of image's left boundary is 10 mm to the right as compared to the position of the end wall and ignition point.

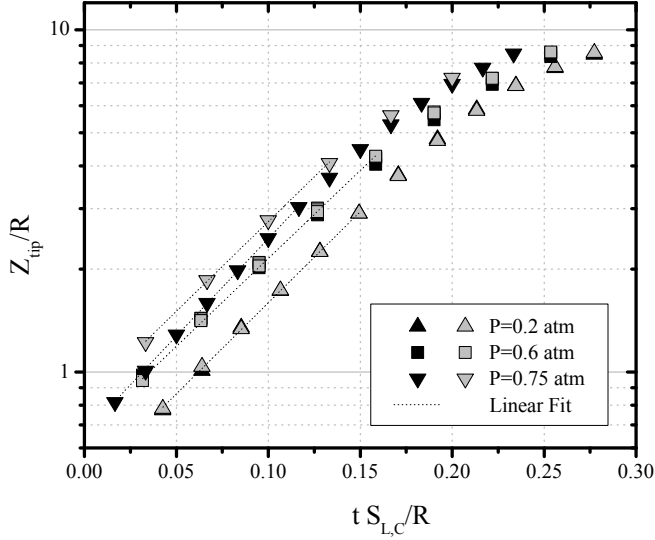


FIG. 7: Scaled flame tip position versus scaled time for different pressures: $P = 0.2$ bar (triangles), $P = 0.6$ bar (squares), $P = 0.75$ bar (upside down triangles). Different color for each pressure correspond to different experimental runs.

tip can be estimated as [2]

$$S_{L,C} = CS_L = S_L \left(1 - L_T \nabla \cdot \mathbf{n} \right) = S_L \left(1 - \frac{2L_T}{R_{tip}} \right). \quad (4.2)$$

As Table I shows, the corrected values of the growth rate $\sigma_{1,C}$ decrease with increasing Ma , while the uncorrected growth rates σ_1 increase instead. This demonstrates a non-negligible effect of pure curvature for low-pressure H_2/O_2 finger flames, disregarding which could reverse the main trend. For this reason, a very accurate determination of the laminar burning velocity is crucial for the analysis of experimental results. This is particularly relevant for extraction of the growth rates σ_1 for various Ma , since even a 15-20% difference in the laminar burning velocity could lead to a completely erroneous conclusion.

B. Numerical results and discussion

We performed direct numerical simulation of flame acceleration in tubes with smooth slip adiabatic walls at different flow parameters. Particularly, we employed planar

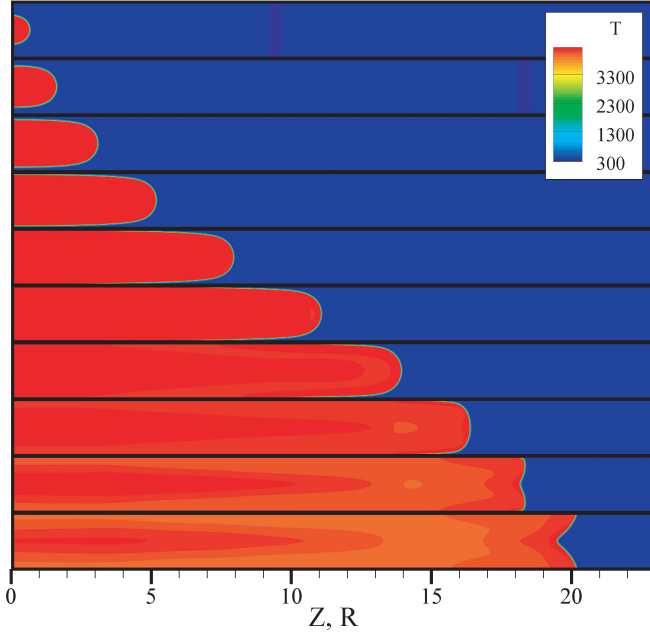


FIG. 8: Temperature field evolution and “tulip” formation for planar geometry, $\Theta = 14$, and Mach number $Ma = 0.005$ at different time instants. Time instants are equally spaced in the range of $(0.04022 \div 0.42161)S_L t/R$.

and axisymmetric geometries, and a range of initial flame propagation Mach numbers $Ma = 10^{-3} \sim 1.6 \times 10^{-2}$. We also used two values of the thermal expansion ratio $\Theta = 8, 14$.

We illustrate evolution of the temperature field for the planar geometry in Fig. 8 for $\Theta = 14$ and the initial Mach number $Ma = 0.005$. The simulation plots also show the instant of transition from a convex “finger” to a concave “tulip” flame shape. It is seen that, similar to the experimental Figure 6, the flame tip curvature does not change significantly from the instant of the transition to finger shape and until the flame skirt touches the wall, thus justifying the assumption of almost constant tip curvature made in Sec. 4 A. It should be noted that formation of finger-shaped laminar flame fronts in planar geometry due to essentially different Schelkin mechanism has been also obtained in simulations of premixed flames in channels with non-slip walls [24, 34]. It is interesting that similar finger front shapes were observed recently within the context of electrochemical doping in organic semiconductors [35], though the leading electrodynamic feedback mechanism is conceptually different as well.

An axisymmetric counterpart of Fig. 8 is presented in Fig. 9 with all parameters being the same except for the geometry. Isosurfaces are shown for $T = 1400K$. Axisymmetric simulations also demonstrate the transition from a convex “finger” to a concave “tulip” flame, accompanied by significant reduction of the flame surface area and propagation velocity. Similar to Figures 6 and 8, the flame tip curvature remains almost constant in a

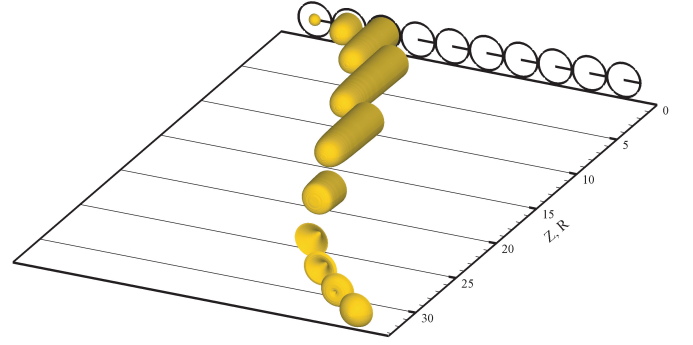


FIG. 9: Flame shape evolution and “tulip” formation for axisymmetric geometry, $\Theta = 14$, and Mach number $Ma = 0.005$ at different time instants. Time instants are equally spaced in the range of $(0.02692 \div 0.26576)S_L t/R$. Isosurfaces are shown for $T = 1400K$.

range of scaled times $\tau_{sph} < \tau < \tau_{wall}$ corresponding to the later stage of finger flame acceleration.

In Fig. 10 we present the scaled flame tip position versus time for the planar geometry for $\Theta = 14$ and the Mach numbers $Ma = 0.001 \sim 0.01$ in both linear and logarithmic scales. We see that the “exponential” nature of acceleration in the planar case is not very pronounced at the early stages, due to the relatively high value of $\tau_{sph} \approx 1/(\Theta - 1)$ compared to its axisymmetric counterpart $\tau_{sph} \approx 1/(2\sqrt{\Theta(\Theta - 1)})$ [12]; the latter being approximately twice smaller for high values of Θ than in the planar case. Figure 11 shows the scaled velocity evolution for $\Theta = 14$ and planar geometry for a set of Mach numbers in the range $Ma = 0.001 \sim 0.01$. Here we see a significant dependence of the maximum flame tip velocity on the initial Mach number. At the same time, Fig. 11 shows that the scaled time of attaining the velocity maximum is almost independent of the Mach number, which can be demonstrated analytically, as follows. If we write the first-order correction to ξ_{tip} in the form $\xi_{tip} = \xi_{tip,0} + Ma\xi_{tip,1}$, where $\xi_{tip,0}$ is given by Eq. (2.14), then Eq. (2.31) becomes

$$\begin{aligned} \vartheta &= \Theta - Ma(\gamma - 1)(\Theta - 1)^2(\xi_{tip,0} + Ma\xi_{tip,1} + 1) \approx \\ &\approx \Theta - Ma(\gamma - 1)(\Theta - 1)[\Theta \exp((\Theta - 1)\tau) - 1]. \end{aligned} \quad (4.3)$$

Similarly, replacing τ in Eq. (4.3) by τ_{wall} in the form $\tau_{wall} = \tau_{wall,0} + Ma\tau_{wall,1}$, we find

$$\vartheta_{wall} \approx \Theta - Ma(\gamma - 1)(\Theta - 1)(\Theta^2 - 1). \quad (4.4)$$

Substituting Eq. (4.4) into Eq. (2.11), we obtain the estimation of τ_{wall} in the compressible case for planar ge-

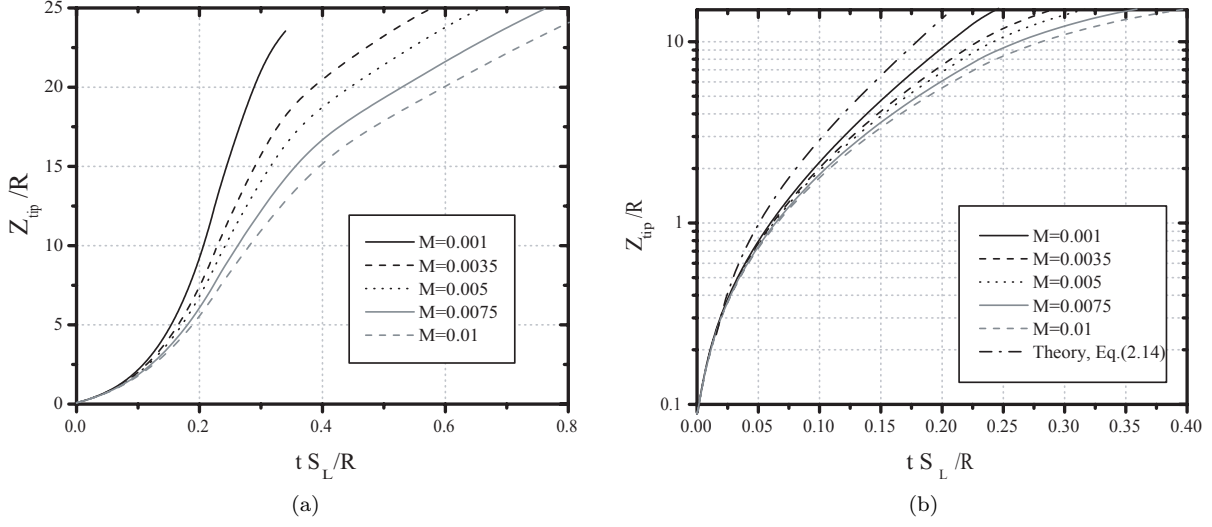


FIG. 10: Scaled flame tip position versus time for planar geometry, $\Theta = 14$, and Mach numbers $Ma = 0.001, 0.0035, 0.005, 0.0075, 0.01$: (a) linear scale, (b) logarithmic scale.

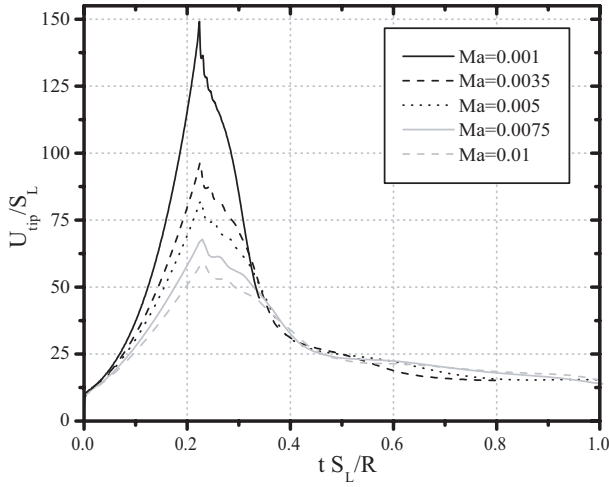


FIG. 11: Scaled velocity of flame tip versus time for planar geometry, $\Theta = 14$, and Mach numbers $Ma = 0.001, 0.0035, 0.005, 0.0075, 0.01$.

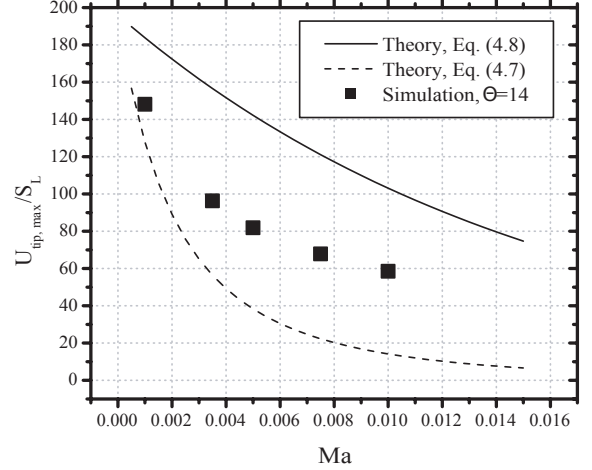


FIG. 12: Scaled maximum flame tip velocity versus Mach number obtained in simulations for planar geometry, $\Theta = 14$, is compared to theoretical estimates. Solid line - Eq. (4.8), dashed line - Eq. (4.7)

ometry:

$$\begin{aligned} \tau_{wall} &= \frac{\ln \vartheta}{\vartheta - 1} \approx \\ &\approx \frac{\ln \Theta}{\Theta - 1} \left[1 + Ma(\gamma - 1)(\Theta^2 - 1) \left(1 - \frac{\Theta - 1}{\Theta \ln \Theta} \right) \right]. \end{aligned} \quad (4.5)$$

For typical $\Theta \approx 5 \sim 10$ and $\gamma \approx 1.4$, the last term in Eq. (4.5) can be approximated as $\sim 0.2Ma\Theta^2$. Consequently, for small Mach numbers $\tau_{wall} = \ln \vartheta / (\vartheta - 1)$ only slightly depends on Ma , which is substantiated by the simulation results of Fig. 11. The weak dependence of τ_{wall}

on Ma is convenient for evaluating the total time of the finger-type flame acceleration. We see from the simulation results of Figure 11 that the instant of the maximum flame tip velocity τ_{wall} only slightly grows with increasing Ma , remaining in the range $\tau_{wall} = 2.2 \sim 2.3$. Using the simplified analytical expression for τ_{wall} we may also estimate maximum flame tip velocity from Eq. (2.40) and Eq. (2.43).

The peculiar feature of concurrent maximums of flame tip velocity for various initial Mach numbers can act as a useful criterion for the validity of S_L and Ma determined in the experiments. While in the numerical simulation

we set Ma as a parameter and obtain the concurrence of maximum tip velocities mentioned above implicitly, analysis of the experimental data could encounter significant difficulties due to the uncertainty of S_L , as discussed in 4 A. Since S_L is used for scaling time and velocity, even a small inaccuracy in its determination could lead to considerable shifting of the maximums of the tip velocity relative to each other. Thus, if the experimental conditions imply $R \approx R_{tip} \gg L_f$, i.e. pure curvature effect on flame tip velocity is insignificant at the later stages of flame acceleration, the concurrence of scaled flame tip velocity peaks could serve as an indication of correctly determined S_L values for different Ma .

It is noted that, similar to the experiments, in the present numerical simulations the initial flame velocity of a hemispherical flame front is considerably affected by pure curvature effect, which can be seen from Figure 11 for the flame tip velocity taken at $tS_L/R = 0$. The initial flame ball radius in the numerical simulations is equal to $R_{init} = 4.0L_f$; thus, similar to Eq. 4.2, we can estimate the correction to the initial flame velocity $S_{L,init}$ in the planar case, with the curvature term $\nabla \cdot \mathbf{n} = 1/R_{init}$ in the form:

$$\frac{S_{L,init}}{S_L} = 1 - \frac{L_f}{R_{init}} = \frac{3}{4}, \quad (4.6)$$

For $\Theta = 14$, the initial tip velocity in the laboratory reference frame is $U_{tip}/S_L = \Theta S_{L,init}/S_L = 0.75\Theta = 10.5$, which is close to that observed in Figure 11. However, the effect of pure curvature does not affect presentation of the data in the present numerical simulations considerably, since we have taken relatively large channel widths corresponding to $R = 50L_f$ in the planar case, as specified in Sec. 3. This renders pure curvature effects negligible for all simulation runs.

Figure 12 shows the scaled maximum flame tip velocity versus the Mach number for the planar geometry and $\Theta = 14$. Analytical estimates for the maximum flame tip velocity shown in Figure 12 are calculated as follows. The first theoretical estimate for the maximum flame tip velocity accounts for all nonlinear terms of Eq. (2.40) and employs the exact solution, Eq. (2.45), as

$$\frac{U_{tip,max}}{S_L} = -Ma\gamma(\Theta - 1)^2 \xi_{tip,wall}^2 + \sigma_1 \xi_{tip,wall} + \Theta_1, \quad (4.7)$$

where $\xi_{tip,wall}$ is the flame tip position at time τ_{wall} calculated from Eq. (2.45), with $\tau = \tau_{wall}$. The second estimate is somewhat simplified accounting for the linear term only; it is derived from Eq. (2.43) as follows:

$$\frac{U_{tip,max}}{S_L} = \sigma_1 \xi_{tip,wall} + \Theta_1, \quad (4.8)$$

with $\xi_{tip,wall} = (\Theta_1/\sigma_1)[\exp(\sigma_1\tau_{wall}) - 1]$. It is seen from Figure 12 that predictions of the complete analytical solution, Eq. (4.7), and the solution accounting for the linear term only, Eq. (4.8), differ significantly, with

the results of numerical simulation lying closer to the exact solution of Eq. (4.7). Most importantly, we see that both the simulation and theoretical results show significant reduction of the scaled maximum flame tip velocity with the increase in the initial Mach number, despite the fact that the non-scaled maximum tip velocity could be still increasing with the initial Mach number. Figure 12 shows that the influence of gas compressibility is not negligible for estimation of the maximum flame velocity for finger-type flame acceleration. Previous theoretical studies [11, 12] did not account for significant reduction of the maximum scaled tip velocity for high initial Mach numbers, since they were conducted for slow methane-air flames. For this reason, the effect of compressibility did not manifest itself in the previous studies.

We next investigate acceleration of the finger-shaped flames at different values of the initial Mach number for the axisymmetric geometry. Fig. 13 shows scaled flame tip position versus time for the axisymmetric geometry for $\Theta = 14$ and the Mach numbers $Ma = 0.001 \sim 0.01$ in both linear and logarithmic scales. It is seen that the stage of exponential flame acceleration is more distinctive in the axisymmetric geometry as compared to the planar case of Fig. 10. Figure 14 is an axisymmetric analogue of Fig. 11. Similar to the planar case, the maximum flame tip velocity strongly depends on the initial Mach number, but the time τ_{wall} , when the maximum flame tip velocity is achieved, depends on Ma slightly. For $\Theta = 14$ used in the simulations of Fig. 14, we have $\alpha \approx 13.5$, and Eq. (2.49) yields $\tau_{wall} \approx 0.15$. The numerical simulations of Fig. 14 shows somewhat delayed maximums of flame tip velocity with $\tau_{wall} \approx 0.2$, as compared to the theoretical prediction. This delay is attributed to the fact that for the axisymmetric case the effect of pure curvature is more pronounced in the initial stage of finger flame propagation, since the axisymmetric counterpart of Eq. (4.6) yields

$$\frac{S_{L,init}}{S_L} = 1 - \frac{2L_f}{R_{init}} = \frac{1}{2}. \quad (4.9)$$

However, in the axisymmetric case we have a wide domain with $R = 75L_f$, see Sec. 3, which renders pure curvature effect at the later stage of finger flame acceleration negligible for all numerical runs in the axisymmetric case, resulting in concurrent peaks of the flame tip velocity in Figure 14, similar to the planar case.

An axisymmetric counterpart of Fig. 12 is presented in Fig. 15. Contrary to the planar case, the theoretical estimate of the maximum tip velocity presented in Fig. 15 is related to two opposite limiting cases described in Sec. 2 C. The first estimate obtained from Eq. (2.67) as

$$\begin{aligned} \frac{U_{tip,max}}{S_L} &= \{2\alpha_1 \tanh(\alpha_1\tau_{wall}) - \\ &- 2Ma\alpha[1 + \gamma(\Theta - 1)]\} \xi_{tip,wall} + \Theta_1, \end{aligned} \quad (4.10)$$

where the flame tip position $\xi_{tip,wall}$ at $\tau = \tau_{wall}$ is calculated from Eq. (2.68) while σ_1 and Θ_1 are given by

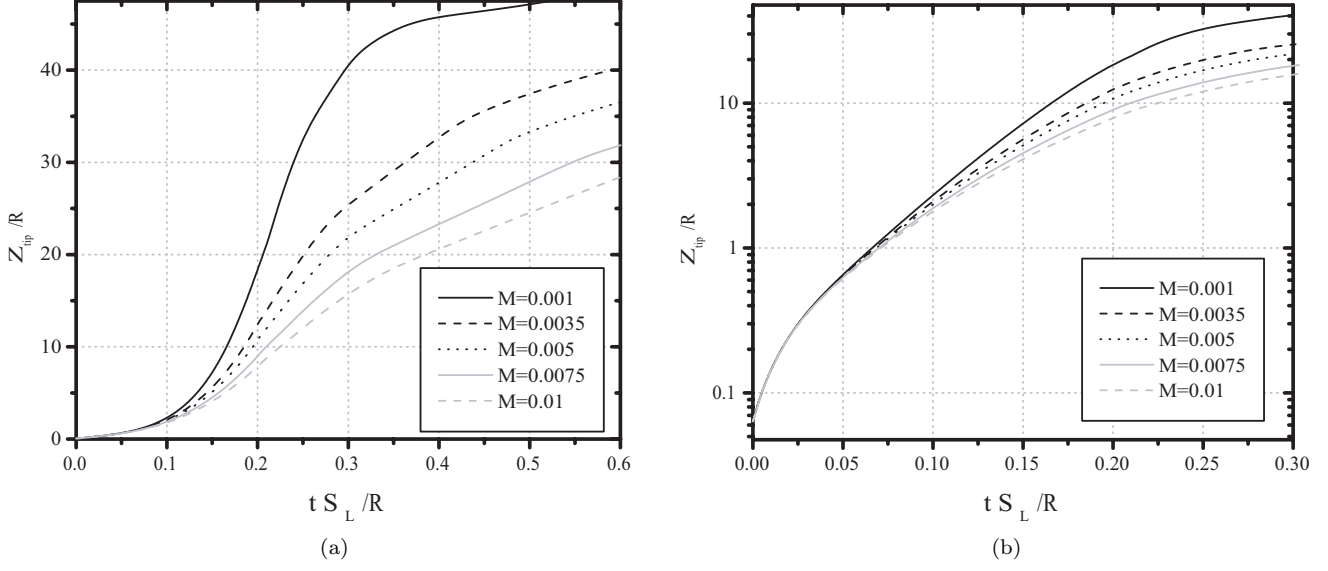


FIG. 13: Scaled flame tip position versus time for axisymmetric geometry, $\Theta = 14$, and Mach numbers $Ma = 0.001, 0.0035, 0.005, 0.0075, 0.01$: (a) linear scale, (b) logarithmic scale.

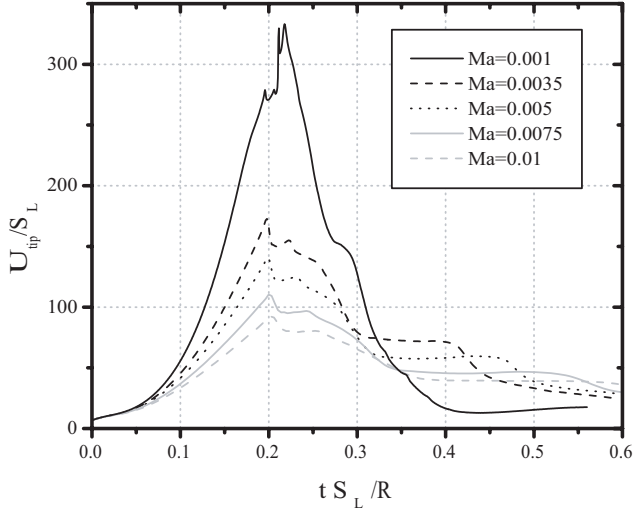


FIG. 14: Scaled velocity of flame tip versus time for axisymmetric geometry, $\Theta = 14$, and Mach numbers $Ma = 0.001, 0.0035, 0.005, 0.0075, 0.01$.

Eqs. (2.71) and (2.65), respectively. For the second limiting case of late stage acceleration, the flame tip velocity estimate is given by Eq. (2.69) as

$$\frac{U_{tip,max}}{S_L} = -2Ma(\Theta - 1)(2\Theta\gamma - \gamma + 1)\xi_{tip,wall}^2 + \sigma_1\xi_{tip,wall} + \Theta_1, \quad (4.11)$$

where the flame tip position $\xi_{tip,wall}$ at $\tau = \tau_{wall}$ is calculated from Eq. (2.72). We see that results of the numeri-

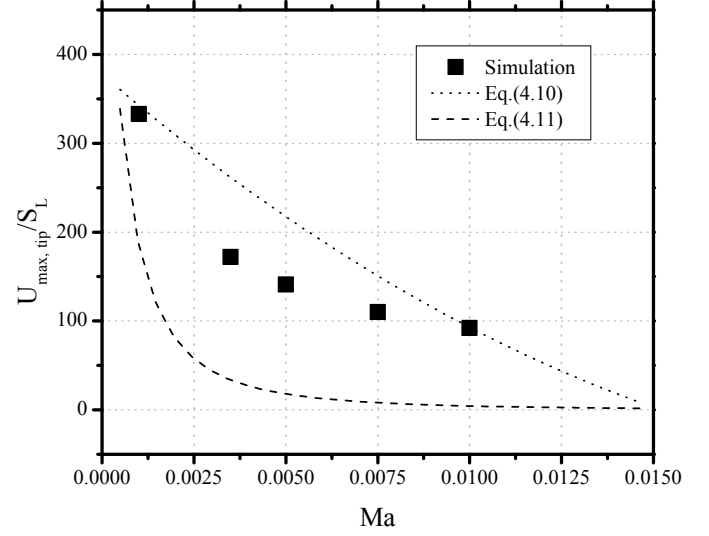


FIG. 15: Scaled maximum flame tip velocity versus Mach number obtained in simulations for axisymmetric geometry, $\Theta = 14$, compared to theoretical estimates of Eqs. (4.10) and (4.11).

cal simulation in most cases are located in between those values given by Eqs. (4.10) and (4.11), as suggested in Sec. 2 C, although, this tendency appears to be changing for higher values of Ma .

Figure 16 shows the scaled acceleration rate versus Mach number for the planar geometry, $\Theta = 8, 14$. It is seen that the agreement of theory and simulations is significantly better for $\Theta = 8$, indicating that the role of gas compressibility increases both with the Mach num-

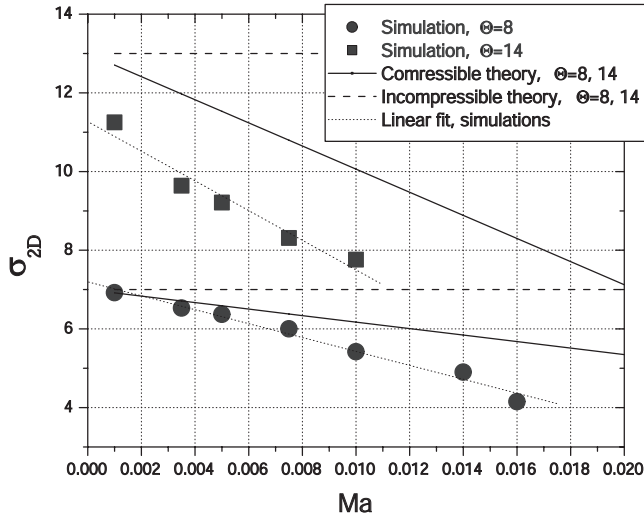


FIG. 16: Scaled acceleration rate versus Mach number for planar geometry, $\Theta = 8, 14$. Values of σ_1 obtained from numerical simulations are shown by circles for $\Theta = 8$ and by squares for $\Theta = 14$. Solid lines correspond to the theoretical dependencies give by Eq. (2.42), dashed line - to incompressible theory, see Eqs. (2.13)-(2.14), dotted lines - to linear fit of simulation data.

ϕ	Θ	S_L , cm/s	c_s m/s	Ma	$1/t$, s $^{-1}$	σ_1
1.0	8.02	41.8	340	0.00123	132.6	15.8
					129.7	15.5

TABLE II: Experimental values of σ_1 obtained from Ref. [11], for $\Theta \approx 8$, low-Mach propane-air mixture and axisymmetric geometry. ϕ is mixture equivalence ratio, c_s is sound speed in unburnt gas mixture, $1/t$ is experimentally measured tulip flame growth rate (for two experimental runs).

ber Ma , and the initial density ratio Θ . Furthermore, Fig. 16 shows that the growth rate σ significantly decreases with increasing Ma , and the isobaric theoretical model of the finger-flame acceleration, Refs. [11, 12], noticeably overestimates the acceleration rate σ for high- Ma flames. We next note that accurate estimate of the acceleration rate is of crucial importance, e.g., for the analysis of flame-generated shocks, preheating of the fuel mixture, pre-detonation run-up distance and the DDT onset [23, 30]. Figure 17 shows the scaled acceleration rate versus the Mach number for axisymmetric geometry, with $\Theta = 8$ and 14. Similar to the planar case of Fig. 16, the agreement of theory and simulations is better for $\Theta = 8$ than for $\Theta = 14$, which indicates a more important role of the compressibility effects for larger Θ . For $\Theta = 14$ we have even more significant deviation of the numerical data from the theoretical predictions as compared to the planar case. Still, the trend remains the same: σ decreases quite rapidly with increasing Ma .

Fig. 18 shows the comparison of scaled acceleration rates obtained in the simulations for the planar and ax-

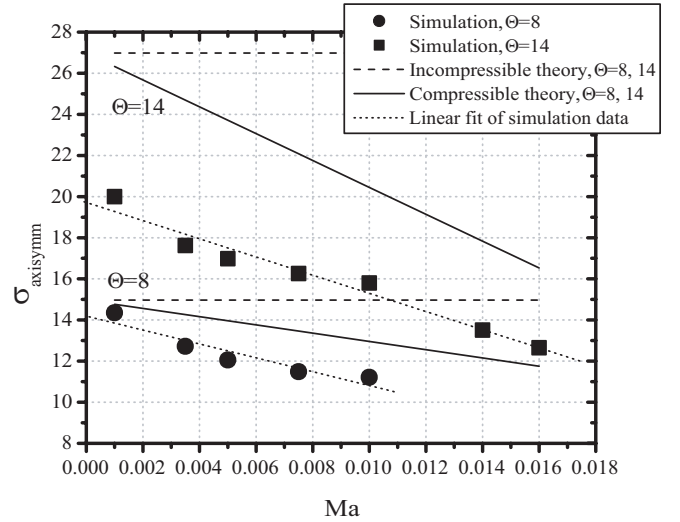


FIG. 17: Scaled acceleration rate versus Mach number for axisymmetric geometry, $\Theta = 8, 14$. Values of σ_1 obtained from numerical simulations are shown by circles for $\Theta = 8$ and by squares for $\Theta = 14$. Solid lines correspond to the theoretical dependencies given by Eq. (2.71), dashed line - to incompressible theory (see Eq. (2.54)), dotted lines - to linear fit of simulation data.

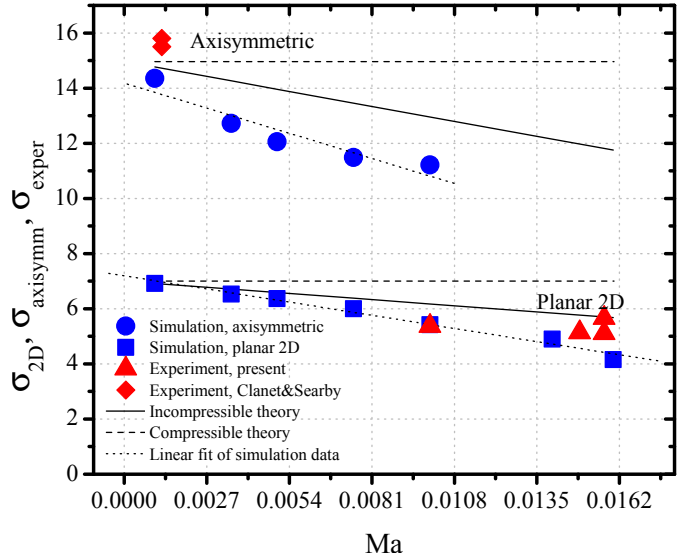


FIG. 18: Comparison of scaled acceleration rates versus Mach number for experiments and simulations for planar and axisymmetric geometries, $\Theta = 8$. Values of σ_1 obtained from numerical simulations are shown by circles for axisymmetric geometry and by squares for planar geometry. Triangles show experimental results of Table I, diamonds - of Ref. [11], see Table II. Solid lines correspond to the theoretical dependencies given by Eq. (2.42) (planar) and Eq. (2.71) (axisymmetric), dashed line - to incompressible theory, see Eq. (2.13) (planar) and Eq. (2.54) (axisymmetric), dotted lines - to linear fit of simulation data.

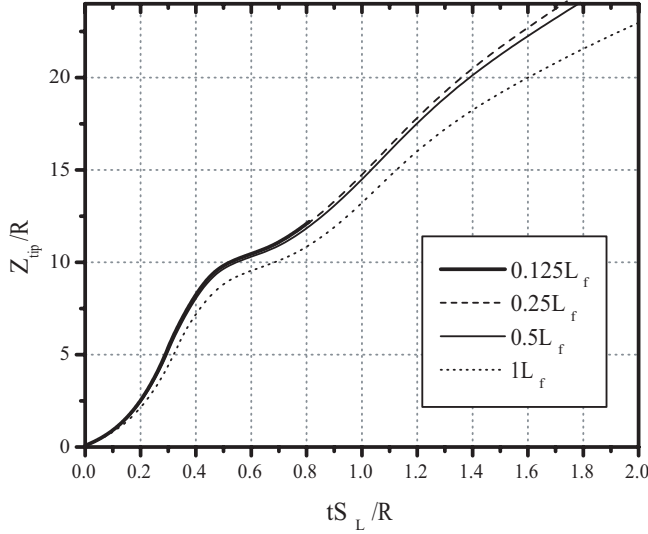


FIG. 19: Flame tip position versus time for different values of the mesh size. Thick solid line correspond to $\Delta z_f/L_f = 0.125$, dashed line - to $\Delta z_f/L_f = 0.25$, thin solid line - to $\Delta z_f/L_f = 0.5$, dotted line - to $\Delta z_f/L_f = 1.0$

isymmetric geometries for $\Theta = 8$; the experimental results for σ_1 obtained in the present work and those of Ref. [11] are also shown. The latter experimental data is summarized in Table II for two experimental runs for neutrally stable ($\phi = 1.0$) low- Ma propane-air mixture with $\Theta = 8.02$, and axisymmetric geometry of the channel. We see from Fig. 18 that the scaled acceleration rate σ_1 obtained in the present experiments for the high- Ma H_2/O_2 stoichiometric mixture in a channel with a quadratic cross-section are considerably closer to the planar case than the axisymmetric one. Thus, although the flame tip has the hemispherical shape, the global flame front acceleration is governed by the quadratic cross-section of the channel and can be described by the theory of Section 2 A. At the same time, values of σ_1 of Table II [11] for low- Ma propane-air mixture are close to the incompressible value σ_0 for the axisymmetric case, in agreement with the present theory. Both the numerical simulation and experimental results indicate that the geometry of the channel affects the growth rate of finger flame acceleration significantly, with the axisymmetric channel being favorable for the faster flame acceleration due to the “finger” flame mechanism.

5. CONCLUSIONS

The theory, experiments and numerical simulations of the present work show that the growth rate σ of the finger-flame acceleration from the closed end of a channel/tube decreases significantly with the increase in initial Mach number, Ma . Hence, previous theoretical estimates of Refs. [11, 12], derived with the incompress-

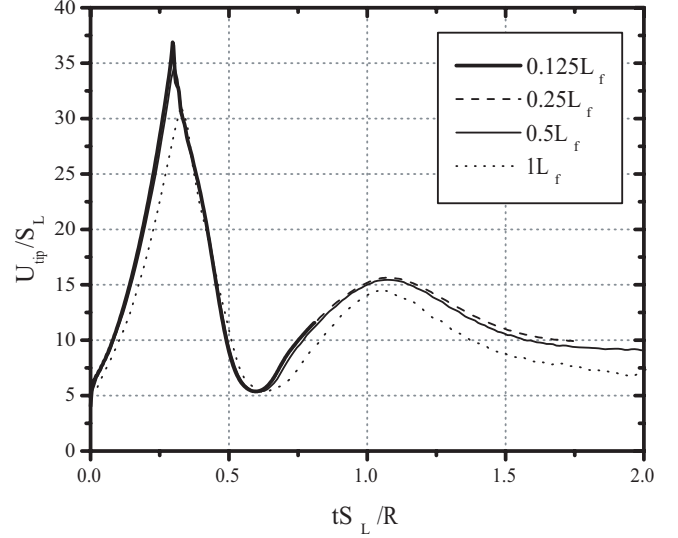


FIG. 20: Velocities of the flame tip versus time for different values of the mesh size. Thick solid line correspond to $\Delta z_f/L_f = 0.125$, dashed line - to $\Delta z_f/L_f = 0.25$, thin solid line - to $\Delta z_f/L_f = 0.5$, dotted line - to $\Delta z_f/L_f = 1.0$

ible approximation, overestimate σ for flames with high laminar burning velocities, such as the H_2/O_2 or acetylene/air flames. In the present study, we account for gas compression in the theory through expansion for small Mach number up to the first-order terms, and validate the theoretical analysis by numerical simulations and experiment. The present numerical simulations and theory show that the maximum flame tip velocity significantly depends on the initial Mach number, with the scaled time of the maximum flame tip velocity being almost independent of Ma . The present results collectively demonstrate that the geometry of the channel affects the growth rate of finger flame significantly, with the axisymmetric channel being more conducive for fast initial flame acceleration from the closed end in channels with smooth walls. Compressibility effects should be taken into account when estimating the strength of shock waves generated by the initial finger-type flame acceleration, preheating of the unburnt fuel mixture ahead of the flame, the DDT onset time and position.

6. ACKNOWLEDGEMENTS

The authors are grateful to Fujia Wu and Hemanth Kolla for useful discussions. This work was supported by the Swedish Research Council (VR) and Stiftelsen Lars Hiertas Minne grant FO2010-1015. Numerical simulations were performed at High Performance Computer Center North (HPC2N), Umeå, Sweden, through the SNAC project 001-10-159.

$\Delta z_f/L_f$	U_{max}/S_L	$\Delta U_{max}/S_L$	$t_{max}S_L/R$	$\Delta t_{max}S_L/R$	$Z_{tip,*}/R$	$\Delta Z_{tip,*}/R$
1.0	31.14		0.3265		4.5095	
0.5	34.68	3.54	0.3032	0.2706	5.282	0.7725
0.25	36.171	1.43	0.2973	0.0059	5.441	0.159
0.125	36.85	0.679	0.2965	0.0008	5.474	0.033

TABLE III: Resolution tests for planar geometry, $Ma = 0.005$, $\Theta = 8$.

7. APPENDIX: RESOLUTION AND LAMINAR VELOCITY TESTS

In order to check if the adopted resolution is sufficient to study the flame acceleration process, we performed the resolution tests for the primary results of the present paper for $Ma = 0.005$. The grid size in the flame domain varied between $0.125L_f$, $0.25L_f$, $0.5L_f$ and $1L_f$. We checked the velocity of the flame tip at the moments corresponding to the stage of maximum flame tip velocity, as well as the flame tip position at time moment $tS_L/R = 0.303$. The resolution test results are presented in Table III and in Figs 19 and 20.

Notation: $\Delta z_f/L_f$ is the spatial step in the flame grid domain; U_{max}/S_L maximum flame tip velocity (see Fig. (20)); $t_{max}S_L/R$ scaled time moment corresponding to the maximum of flame tip velocity; $Z_{tip,*}/R$ flame tip position at time moment $t_*S_L/R = 0.303$ (see Fig. (20)). $\Delta U_{max}/S_L$ increment of U_{max}/S_L calculated in the table row i as $\Delta U_{max}(i) = U_{max}(i) - U_{max}(i-1)$. Increments

for $t_{max}S_L/R$ and $Z_{tip,*}/R$ are calculated in a similar manner. Resolution in the wave grid domain is equal to $\Delta z_w = 2 \times \Delta z_f$ for each run.

Table III and Figs. 19, 20 show good convergence of the numerical solution with the increase of mesh resolution. Resolution tests also showed convergence of time corresponding to maximum flame tip velocity with the increase of resolution.

In addition to the resolution tests, laminar flame velocity tests were performed for $Ma = 0.001$, $\Theta = 8, 14$. Numerical setup was similar of the main numerical experiments, except for planar initial flame front and tube width $2R = 4L_f$. That value was chosen to be below the critical diameter needed for the growth of the hydrodynamic instability [27], so that the flame front remains planar during the test simulation. For $\Theta = 14$, measured laminar planar flame velocity in laboratory frame was $U_{f, lab}/S_L = 13.97 \pm 0.03$; for $\Theta = 8$ $U_{f, lab}/S_L = 7.97 \pm 0.05$.

-
- [1] Zeldovich Ya. B., Barenblatt G. I., Librovich V. B., Makhviladze G. M. (1985) *The Mathematical Theory of Combustion and Explosions*. New York: Consultants Bureau.
 - [2] Law C. K. (2006) *Combustion Physics*. New York: Cambridge University Press.
 - [3] Roy G.D., Frolov S.M., Borisov A.A., Netzer D.W., (2004) *Prog. Energy Combust. Sci.* **30**, 545
 - [4] Ciccarelli, G., Dorofeev, S. (2008) *Prog. Energy Combust. Sci.*, **34**(4), 499-550
 - [5] Dorofeev S.B. (2011) *Proc. Comb. Inst.*, **33**, 2161-2175
 - [6] Shelkin K., (1940) *J. Exp. Theor. Phys.*, **10**, 823.
 - [7] Bychkov V., Valiev D., Eriksson L.-E., (2008) *Phys. Rev. Lett.*, **101**, 164501.
 - [8] Bychkov V., Petchenko A., Akkerman V., Eriksson L.-E., (2005) *Phys. Rev. E*, **72**, 046307.
 - [9] Akkerman V., Bychkov V., Petchenko A., Eriksson L.-E., (2006) *Combust. Flame*, **145**, 206.
 - [10] Valiev D., Bychkov V., Akkerman V., Law C. K., Eriksson L.-E. (2010) *Combust. Flame*, **157**, 1012-1021
 - [11] Clanet C., Searby G. (1996) *Combust. Flame*, **105**, 225-238.
 - [12] Bychkov V., Akkerman V., Fru G., Petchenko A., Eriksson L.-E. (2007) *Combust. Flame*, **150**, 263-276.
 - [13] Dunn-Rankin D., Sawyer R. F. (1998) *Experiments in Fluids*, **24**, 130-140.
 - [14] McGreevy J. L., Matalon M. (1994) *Comb. Sci. Tech.* **100**, 75-94.
 - [15] Nkonga B., Fernandez G., Guillard H., Larroturou B. (1993) *Comb. Sci. Tech.* **87**, 69-89.
 - [16] Oppenheim A. K., Ghoniem A. F. (1983) In *21st Aerospace Sciences Meeting* AIAA-83-0470. Reno, Nevada.
 - [17] Kuznetsov M., Liberman M., Matsukov I. (2010) *Comb. Sci. Tech.* **182**, 1628 - 1644.
 - [18] Wu M., Burke M., Son S., Yetter R., *Proc. Combust. Inst.* **31**, 2429 (2007).
 - [19] Ciccarelli G., Johansen C., Parravani M. (2010) *Combust. Flame* **157**, 2125.
 - [20] Kuznetsov M., Alekseev V., Matsukov I., Dorofeev S. (2005) *Shock Waves* **14**, 205-215.
 - [21] Landau L. D., Lifshitz E. M. (1993) *Fluid mechanics*. Oxford ; New York: Pergamon Press.
 - [22] Chue R., Clarke J., Lee J.H. (1993) *Proc. R. Soc. Lond. A* **441** 607 .
 - [23] Bychkov V. and Akkerman V., (2006) *Phys. Rev. E* **73**, 066305.
 - [24] Valiev D. M., Bychkov V., Akkerman V., Eriksson L.-E. (2009) *Phys. Rev. E*, **80**, 11.
 - [25] Bychkov V., Akkerman V., Valiev D., Law C. K. (2010) *Combust. Flame*, **157**, 2008-2011.
 - [26] Bychkov V., Akkerman V. Valiev D., Law C. K. (2010) *Phys. Rev. E*, **81**, 026309.
 - [27] Liberman, M.A., Ivanov M.F., Peil O.E., Valiev D.M.,

- Eriksson L.-E. (2003) *Combustion Theory And Modelling*, **7**, Issue 4, 653-676
- [28] Poinot T., Veynante D., 2001. *Theoretical and Numerical Combustion*, R.T. Edwards
- [29] Akkerman V., Bychkov V., Petchenko A., Eriksson L.-E., (2006) *Combust. Flame*, **145**, 675.
- [30] Valiev D., V. Bychkov, V. Akkerman, L.-E. Eriksson (2008) *Phys. Lett. A* **372**, Issues 27-28, 4850
- [31] Wollblad C., Davidson L. , L.-E. Eriksson (2006) *AIAA Journal*, **44**, 2340-2353.
- [32] Kee R.J., Rupley F.M., Miller J.A. (1991) *CHEMKIN-II: A FORTRAN Chemical Kinetics Package for the Analysis of Gas-Phase Chemical Kinetics*, Technical Report SAND89-8009B, UC-706, Sandia National Laboratories, Albuquerque, New Mexico
- [33] Burke M.P. , Chaos M., Ju Y., Dryer F.L., and Klippenstein S.J. (2011) "Comprehensive H₂/O₂ Kinetic Model for High-Pressure Combustion", International Journal of Chemical Kinetics, Accepted for publication
- [34] Kagan L., Sivashinsky G. (2003) *Combust. Flame* **134** 389 .
- [35] Bychkov V., Matyba P., Akkerman V., Modestov M., Valiev D., Brodin G., Law C.K., Marklund M., Edman L. (2011) *Phys. Rev. Lett.* **107**, 016103.